Aging phenomena and their modelling in aqueous organic redox flow batteries: a review.

Loïs Briot[a,1], Marie-Cécile Pera[b], Martin Petit[a], Quentin Cacciuttolo[a]

[a]IFP Energies Nouvelles, Rond-point de l'échangeur de Solaize, BP3, 69390 Solaize, France

[b]FEMTO-ST Institute, FCLAB, Univ. Bourgogne Franche-Comté, CNRS, Belfort, France

Abstract

As world's energy needs increase while the quantity of greenhouse gases rejected in the atmosphere must be restrained, the search for renewable energy sources and for ways to store this energy is growing exponentially. Redox flow batteries, which allow decoupling energy from power, are a promising way of electrochemical storage of electricity. Vanadium flow batteries, the current technological reference, are giving way to aqueous organic electroactive species, which present the advantages of multiple designs thanks to functionalization, lower cost, non-toxicity, and no supply issues. Their long-term performances are still compromised because of degradations of the electrodes, the membrane, or the organic species. Physical models are a good way to predict redox flow batteries behavior on long time scales and have a better understanding of the phenomena and their impact on the battery. Some degradations of the electrodes, the membrane or side reactions have been modeled, however very few models for organic active species degradations have been proposed yet.

This review presents some state-of-the-art results obtained with aqueous organic redox flow batteries, before focusing on the reported degradations and their consequences for the cell components and organic electrolytes. Different existing models for aqueous organic redox flow batteries are presented, with a focus on Multiphysics models. Finally, the modelling of degradations in redox flow batteries is discussed, with existing degradations models as well as some propositions for future degradations modelling.

Keywords: Redox flow batteries, aging, modelling, organic redox flow batteries, degradations

---

[1] Corresponding author

1 Introduction

While modern society tends to decrease its dependence on oil and fossil fuels by developing electric mobility and increasing the share of renewable energy production, its electricity needs are constantly increasing: International Energy Agency (IEA) predicts a doubling of electricity share in the global energy mix, from 27% in 2019 to 60% in 2030 to achieve the "Net Zero Emissions by 2050" scenario [1]. Electricity production and consumption have to be constantly balanced for the grid functioning, but this is harder and harder to achieve with an increasing share of renewable energies in the global electricity mix, as many of them are intermittent by nature (solar, wind) and cannot fit the demand curve. Also, fast response, stability and resilience are needed characteristics for the electricity grid in order to avoid power failures as it happened in the past [2,3]. Energy storage with redox flow batteries (RFBs) can help solving both of these issues, by creating a buffer between renewable generation of electricity and consumption, and also by offering a flexible and fast responding resource to grid operators for a better fit of electricity needs.

Several energy storage solutions are currently used at different scales. Among them, pumped hydro and compressed air storage share the biggest volume of stored energy with more than 96% of the total storage capacity installed worldwide in 2018 [4]. Electrochemical energy storage comprises different types of batteries, which are a good choice for smaller storage applications due to their versatility of use, their high power to size ratio and their good efficiency. Furthermore, they do not need special terrain to be used, as do pumped hydro and CAES, and have a lower capital cost. Redox flow batteries in particular can be of great use in large-scale stationary energy storage (10 kW – 10 MW), thanks to their cost, flexibility, depth of discharge, rapid response and safety advantages compared to other technologies [5]. They can have numerous applications, from load levelling or peak shaving to emergency backup solutions.

Redox flow batteries (RFBs) are open electrochemical systems where electrolyte flows from tanks to electrodes (Figure 1). A unitary flow cell is composed of two electrodes, current collectors, and a membrane. Electrodes are usually modified carbon felts where electrochemical reactions take place at the interface with the electrolyte [6]. Current collectors or bipolar plates are graphite-based plates where the electrons flow to and from the external electrical circuit. The membrane separates the negative from the positive electrode so as to avoid any mixing, it is electronically insulating to avoid short-circuits, while allowing the crossing of certain ions – usually either anions or cations – to ensure global electrical neutrality in the cell [7]. Electroactive species are dissolved in liquid electrolytes (posolyte and negolyte) which are stored in external tanks and pumped through the carbon electrodes. The original aspect of redox flow batteries in comparison with conventional batteries is that electroactive materials are stored externally from the electrodes, which allows decoupling energy (driven by volume and concentration of the electrolytes) and power (governed by the electrodes size).
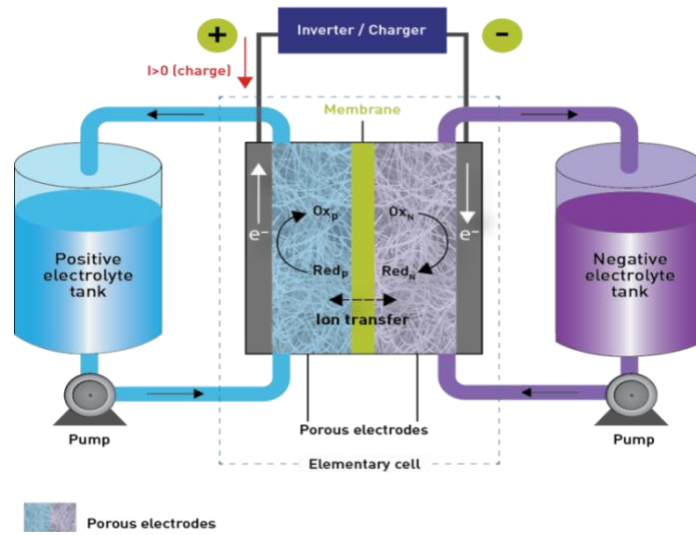
Figure 1 Redox flow battery scheme

Several parameters are used to describe the performances of a battery [8–10]. Table 1 describe the most common parameters used when it comes to evaluate the performances of redox flow batteries.

Table 1 Macroscopic key parameters for redox flow batteries operation

Physical parameter	Formula	Target value in RFBs
Cell Voltage (V)	$U_{cell} = E_{pos} - E_{neg} - \eta^{kinetics} - \eta^{res}$	1 – 1,5
Volumetric capacity (Ah.L^{-1})	$Q_{vol} = \dfrac{zCF}{3600} = 26,8 . zC$	100
Energy density (Wh.L^{-1})	$E_{v,discharge} = \dfrac{1}{(V_{pos} + V_{neg})} \int I_{discharge} . U_{cell} . dt$	150
Max power density (W.cm^{-2})	$P = \dfrac{U_{cell} I}{S}$	1
Electrolyte utilization	$EU = \dfrac{Q_{exp}}{Q_{th}}$	>75%
Capacity fade rate	$\dfrac{\Delta Q_{cell}/\Delta t}{Q_{cell}}$	<0.01% per day or <0.002% per cycle
Coulombic efficiency – CE	$CE = \dfrac{Q_{discharge}}{Q_{charge}}$	>99.9%
Energy efficiency – EE	$EE = \dfrac{E_{v,discharge}}{E_{v,charge}}$	>75%

Theoretical cell voltage is the difference of potential between the positive E_{pos} and the negative E_{neg} electrodes, but the actual voltage U_{cell} also includes inner resistance of the cell and kinetic overpotentials. Volumetric capacity of an electrolyte Q_{vol} is the amount of charge stored in the electrolyte, determined by the concentration of the electroactive species C (mol.L^{-1}) and the number of electrons exchanged in the redox reaction z. F is the Faraday constant (C.mol^{-1}), representing the amount of charge in one mole of electrons. Theoretical capacity of the cell $Q_{cell,th}$ is equal to the lowest capacity between posolyte and negolyte. Energy density of a cell represents the amount of energy that can be stored in the entire cell [11]. It is homogeneous to a capacity density multiplied by the voltage of the cell. When estimating the energy density, the voltage U_{cell} (V) is usually the mean discharge voltage. The product is divided by the sum of the two volumes, corresponding to the total electrolyte volume in the cell. This proposed way of calculating the energy density, is not always a consensus among researchers. Examples of calculations

without taking into account the volume of both electrolytes are often found in the literature which, although not false, lead to overestimated energy density estimations at the process scale [8,12]. Power density represents the maximum power per surface area of electrode that the battery can deliver. I is the current flowing through the external circuit (in A) and S the active surface area of the electrodes (in cm^2). Power density is mainly affected by the redox potentials, conductivities of the cell, kinetics of redox reactions and mass transport. Electrolyte Utilization is the ratio between experimental and theoretical capacity of a cell. This parameter, although important, is not yet systematically reported in scientific experiments [13]. The capacity fade rate of a battery is an essential parameter to estimate aging. Coulombic efficiency (CE) is the ratio between the charge delivered during discharge and the charge accumulated during charging of the battery. Voltage efficiency (VE) is the ratio between the average charge voltage and the average discharge voltage. Energy efficiency (EE) is the ratio between the delivered energy during discharge and the stored energy during charge. EE is the product of CE with VE. At process scale, pumping losses diminish the energy efficiency.

The redox flow battery technology appeared in the 1970s with the development of Fe/Cr RFB by the NASA [14]. Traditional RFBs developed afterwards use inorganic compounds as redox active species such as zinc, lead-acid, bromine or polysulfides [15]. Among inorganic species, the most promising is vanadium as it exists in many different oxidation states, has good redox properties and excellent stability; it is still today the reference technology for RFBs with a large majority of the commercial applications [16–25]. This is mainly due to the simplicity of the system, its relatively low cost, good redox properties and excellent stability [27]. The particularity of VRFB compared to other batteries are that the same element, vanadium, is used as electroactive material on both sides of the cell, exploiting all its oxidation states. VO^{2+} (V^{4+}) and VO_2^+ (V^{5+}) react at the positive electrode (Equation 1), V^{2+} and V^{3+} at the negative electrode (Equation 2).

$$VO^{2+} + H_2O \leftrightarrow VO_2^+ + 2H^+ + e^-$$
<div align="right">Equation 1</div>

$$V^{3+} + e^- \leftrightarrow V^{2+}$$
<div align="right">Equation 2</div>

The operating cell voltage is between 1.4 V and 1.6 V, with one exchanged electron [28]. The resulting typical energy density of the redox flow cell is between 25-50 $Wh.L^{-1}$ [13]. A high power density and stable battery has been developed and can be cycled 20,000 times at 600 $mA.cm^{-2}$, with an energy efficiency of 80%, and maximal power density of 2.78 $W.cm^{-2}$ [29]. The cost of all-vanadium batteries depends on several factors, and is estimated between 300 – 700 $.kWh^{-1}$ [28]. Several examples of demonstration systems have been developed (in the kW/kWh to MW/MWh range), some listed in a review about advances around vanadium batteries from Skyllas-Kazacos *et al.* in 2009 [30]. Known difficulties using vanadium species are their operation in strong acidic environment, their low thermal stability, the high cost of vanadium, as well as the formation of vanadium pentoxide V_2O_5 which can precipitate upon operating the battery and is quite hard to dissolve again [26,27]. Though crossover of vanadium species is an issue, its impact is reduced because the electrolytes can be regenerated through remixing. This strategy allows for very long lasting electrolytes, but the remixing process results in an unavoidable punctual loss in efficiency [32].

Other inorganic technologies have been developed, either "liquid-based" with electroactive species dissolved in the electrolytes or "hybrid", with at least one active material in a solid or gaseous form under one of its state of charge. Overall, inorganic based RFBs face several limits, which often include high price, criticity of the used materials, hazardousness, toxicity for human beings and the environment, low kinetics, or crossover. To try and solve these issues, organic redox flow batteries (ORFBs) are being developed since 2009 [28]. Such batteries employ organic molecules dissolved in aqueous or organic solvents to

store energy, instead of inorganic materials. This technological breakthrough aims at producing sustainable, environment benign and potentially cheap redox flow batteries [29,30].

During battery operation, performance losses cannot be avoided and must be minimized or at least controlled. They are the consequence of several phenomena including crossover, side reactions, degradation of the cell components, etc. Understanding these phenomena is essential to mitigate them, but the study of some of them is harder in the laboratory because they appear on the course of long timescales and the required equipment for their investigation is expensive. Knowing how they affect the battery's performances can help to study degradations with dedicated accelerated aging tests. A commonly used tool to explore these degradation reactions schemes in order to foresee the capacity or power fade of the battery, in combination with experimental work, is through modelling the system and its degradations [31]. Redox flow batteries models already exist for inorganic technologies, and are based on other electrochemical devices' models, such as PEMFC, lead-acid or lithium-ion. Several types of models exist, from empiric to physical-based, and can be applied at different scales. However, there is a lack of modelling works focusing on organic species degradations.

This review aims at gathering the existing state of the art on aqueous organic redox flow batteries degradations and its modelling. The main degradations occurring in the cell unit (i.e. membrane, electrodes) are discussed, and some common degradations of the electroactive organic species encountered in the literature are also listed. A summary of the degradations' classification is proposed, which can serve as basis for their modelling, as well as common experimental investigation methods for qualifying and quantifying the degradations. The last section is dedicated to a presentation of redox flow battery modelling with a focus on physical models and gives some insights for modelling the degradations.

2 Organic redox flow batteries aging

2.1.1 Organic redox flow batteries

The emergence of organic electroactive species is due to the great variety of possible structures, associated with the ability to functionalize them and thus enhance certain useful properties [47]. Furthermore, organic redox materials usually benefit from fast kinetics, thus enabling to dispense with the use of a catalyst as in some inorganic RFBs [9]. Developing "all-organic" redox flow batteries, i.e. organic electroactive species in organic media, enables to access a higher cell voltage thanks to the wider electrochemical window of up to 5 V, as one would get rid of the water electrochemical activity. However, severe drawbacks in terms of security of operation and power density, which are poor in these media, limit the development of all-organic redox flow batteries. The hurdle is to obtain decent conductivity, to lower the high resistance between electrolyte and separator and to enhance the chemical stability of species at a lower cost [32]. Furthermore, the cost for operation and maintenance is higher when working in organic media. In this review we chose to consider only aqueous organic redox flow batteries (AORFBs), the reason being their simplicity of use and better power and stability performances associated with increased safety.

Major families of organic molecules for aqueous RFBs are organometallics – mostly ferrocyanide and ferrocene -, quinones, viologens, (2,2,6,6-Tetramethylpiperidin-1-yl)oxyl (TEMPO), phenazines and alloxazines. These species, presented in Table 2, have been studied in RFBs applications for about a decade, and promising results have been achieved. Table 3 shows some key examples of performances for aqueous organic redox flow batteries, at laboratory scale.

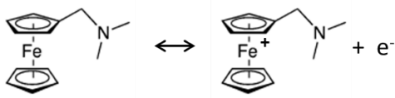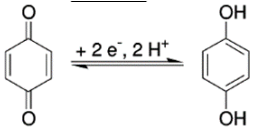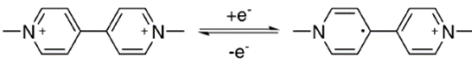**Table 2 Main organic families used as electroactive species in ORFBs**
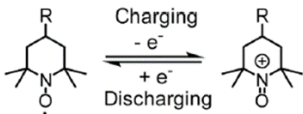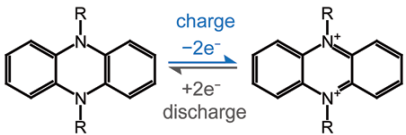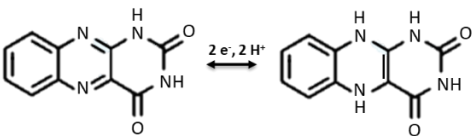
Family	Formula	Characteristics
Ferrocyanide [33]		• 1 e⁻ transfer • $E^0 = 0.5V$ vs. SHE • Light-sensitive
Ferrocene [34]		• 1 e⁻ transfer • Stable • Low solubility
Quinone [35]		• 2 e⁻ transfer • High solubility • Structural diversity (benzoquinones, naphthoquinones, anthraquinones)
Viologen [36]		• Theoretical 2 e⁻ transfer • Irreversible 2nd e⁻ transfer without functionalization • High solubility at neutral pH
TEMPO [37]		• 1 e⁻ transfer • $E^0 = 0.8 – 1.1$ V vs. SHE • Low solubility without functionalization
Phenazine [38]		• 2 e⁻ transfer • Low solubility without functionalization • Easy synthesis • Structural diversity
Alloxazine [39]		• 2 e⁻ transfer • Low solubility without functionalization

Table 3 Examples of aqueous organic redox flow battery full cell results

Negolyte	Posolyte	pH	Results	Reference
2,6-AQDS (1M)	4,5-BQDS (1M)	1	• U_{cell} = 0.9 V (0.7 V later), j = 100 mA.cm^{-2} • EU = 33%, CE > 100% (after the 1st cycle), EE = 70% • No crossover after 100 cycles but degradations (Michael addition)	[40]
2,6-DHAQ (0.5 M)	K$_4$Fe(CN)$_6$ (0.4 M)	14	• U_{cell} = 1.2 V, j = 100 mA.cm^{-2} • CE > 99%, EE > 84% • Capacity retention: 90% after 100 cycles	[41]
2,6-DPPEAQ (0.5 M)	K$_4$Fe(CN)$_6$ (0.4 M)	9	• U_{cell} = 1 V, j = 100 mA.cm^{-2} • EU = 97%, CE > 99.9% • Capacity retention: 99.83% after 480 cycles	[42]
Methyl viologen (0.5 M)	4-HO-TEMPO (0.5 M)	7	• U_{cell} = 1.25 V, j = 60 mA.cm^{-2} • EU = 71.5%, CE > 99%, EE > 60% • Capacity retention: 89% after 100 cycles	[43]
BTMAP-Viologen (1.3 M)	BTMAP-Ferrocene (1.3 M)	7	• U_{cell} = 0.7 V, j = 50 mA.cm^{-2} • CE > 99.95% • Capacity retention: 98.58% after 250 cycles	[44]
(SPr)$_2$V (0.9 M)	(NH$_4$)$_4$Fe(CN)$_6$ (0.9 M)	7	• U_{cell} = 0.82 V, j = 40 mA.cm^{-2} • EE = 62.6% • No reported capacity fade after 1,000 cycles	[45]
DHPS (1.4 M)	K$_4$Fe(CN)$_6$ (0.6 M)	14	• U_{cell} = 1.4 V, j = 100 mA.cm^{-2} • EU = 90%, EE = 82% • Capacity retention: 90% after 500 cycles	[38]
ACA (0.5 M)	K$_4$Fe(CN)$_6$ (0.4 M)	14	• U_{cell} = 1.1 V, j = 100 mA.cm^{-2} • CE > 99%, EE = 63% • Capacity retention: 91% after 100 cycles	[39]

The examples of full cell performances shown in Table 3 must be considered carefully, as the results depend a lot on experimental conditions. These include (but are not limited to) operating atmosphere (argon or nitrogen atmosphere vs. air), type of membrane used, reactants concentrations (which are sometimes much lower than their expected solubility), operating voltage window, current density, charge-discharge protocol (potential holds at the end of each phase or not) etc. The performances must also be compared with regards to the expected cost of each electrolyte, determining the viability of the redox flow battery.

2.2 Aging mechanisms of aqueous redox flow batteries

Performance degradation in aqueous redox flow batteries are due to degradation of the cell internal components, namely electrodes, bipolar plates, and membrane, as well as aging of electroactive species. Aging mechanisms for the cell components of an ORFB are essentially the same than in traditional

inorganic redox batteries and are quite well documented for the VRFB case. They are also largely inspired from the fuel cells aging literature. These degradations can occur at the electrodes or bipolar plates (similar degradations due to the same nature of materials used), or at the membrane. Aging of electroactive organic species can be either of a chemical nature, resulting in so-called "calendar aging" or aging without cycling, or it can be electrochemical, resulting in a performance decrease upon cycling the battery.

2.2.1 Degradations of electrodes and bipolar plates

Mechanical degradation of the electrodes induces reduced active surface area or a change in the electrodes' porosity [46]. Derr *et al.* studied both the chemical [47] and electrochemical [48] degradation of carbon felt electrodes in a VRFB, using Electrochemical Impedance Spectroscopy (EIS) and XPS [49]. They noted oxidation on both half cells, unexpectedly since the potential of the negative half-cell never exceeded the standard potential for carbon oxidation. The oxygen functional groups produced with oxidation of the electrodes had a significantly higher impact on the negative electrode. Carbon corrosion induces a change in the electrode pore structure [50]. However, Nourani *et al.* stated that this corrosion overall enhances VRFB performance by increasing active surface area and hydrophilicity of the electrodes, acting like a surface treatment of the carbon electrode [51]. At the positive electrode, CO_2 formation is a possible reaction to avoid in aqueous media. Current collectors, or bipolar plates, are mostly affected by the electrochemical corrosion due to the acidic electrolyte [52]. This corrosion can be neglected when operating in neutral or alkaline environment, conditions more and more frequently encountered thanks to the design of new organic species stable in these media.

Treatments are available to prevent several reactions or get the electrodes back to their pristine form. These include ex-situ thermal treatments or reduction reaction for example. The use of noble metal catalysts, stable in acidic conditions, were also reported for the negative electrode. However, noble metals such as platinum or gold catalysts cannot be practically used because they catalyze hydrogen or oxygen evolution reaction, which are not desired in these redox flow systems [49].

2.2.2 Aging mechanisms of the membrane

Degradations of the membrane can be either mechanical, chemical, or electrochemical. Mechanical constraints are applied on the membrane if the pressure is too high, or in case of swelling of the membrane or the electrodes [53]. These constraints can lead to cracks or punctures in the membrane.

Hydrogen peroxide formation can be formed similarly as in fuel cells, with subsequent radical formation via Fenton reaction [54]. Such radicals can attack the membrane's polymer side-chains, provoking chemical degradation of the fuel cells membranes [55]. Chemical degradation also happens for vanadium redox flow batteries membranes, and is caused by oxidation of the membrane by catholyte species [52]. Ex-situ studies showed that SSC polymer membranes (e.g. Aquivion®) are less sensitive to radical attacks than LSC polymer membranes (e.g. Nafion®) [56]. Water transfer through the membrane is another issue, which can lead to precipitation of active species if their concentration exceed their solubility [57]. It has been demonstrated that the direction of the water flux depends on the SOC range of the study and the type of membrane used, AEM or CEM. This water transfer seems to be mainly caused by diffusion. The electro-osmotic drag of water and hydraulic permeation are considered negligible in the entire process, as the results modelled by Oh et al. suggest [58].

Crossover, although not being strictly a membrane degradation, is an aging mechanism partly related to the membrane properties. It is usually the predominant cause for performance degradation in inorganic RFBs but is lower in organic RFBs because of the higher steric hindrance of organic molecules compared to inorganic materials. Crossover of MV and TEMPO through different membranes by diffusion, migration and electroosmotic drag was studied [59]. They found that the diffusion rate in the membrane was not the main parameter for crossover, and the most diffusive membranes showed less crossover due to a reduced electroosmotic drag. Thus, the parameters to look for in a membrane along with diffusion coefficients of species are water uptake and ion exchange capacity, as the latter and a high water content mean both

less electroosmotic drag and less crossover. Crossover can be reduced with modified operation parameters, such as increasing membrane thickness, operating at a higher current density or reducing the electrodes active area [10].

2.2.3 Side reactions occurring in aqueous redox flow batteries

In aqueous redox flow batteries, the main side reactions occurring are related to the electrochemical reactions of water. Oxygen evolution reaction (OER) and Hydrogen evolution reaction (HER) happen on the positive and negative electrode, respectively, when potentials approach the solvent's electrochemical stability limits. These reactions almost exclusively take place during the charging process, and induce a decrease in the active surface area [48]. For example, reactions are presented below at pH 14:

$$4OH^- \rightarrow O_2 + 4e^- + 2H_2O \qquad E_{OER}^0 = 0.4\ V \qquad \text{Equation 3}$$
$$2H_2O + 2e^- \rightarrow 2OH^- + H_2 \qquad E_{HER}^0 = -0.8277\ V \qquad \text{Equation 4}$$

These reactions are voltage-dependent, thus special care must be taken to stay within electrochemical stability window of water. Furthermore, oxygen and hydrogen evolution can induce pH fluctuations, which can lead to further degradation reactions for electroactive species [40].

Another side reaction observed in vanadium flow batteries is carbon oxidation to form CO_2 [52]. This reaction not only decreases CE of the battery, but it also changes the electrode structure because of the oxygen reaction with carbon. However, this is known to happen in highly acidic environment and is therefore not a major degradation in most organic redox flow batteries.

2.3 Aging mechanisms specific to aqueous organic redox flow batteries

Aqueous organic redox flow batteries development is at an early stage, mainly because of the performance's losses occurring upon operation of the batteries. Losses can be attributed to several degradation factors, but the predominant are those directly concerning the use of new organic electroactive material. The degradations of quinones, organometallics, viologens and TEMPO have been explored for a few years now, but only few of these degradations have been studied in the frame of redox flow battery operation. This section will attempt to make a listing of the reported aging mechanisms in the literature for those organic molecules. Similar reports have been made by Liu *et al.* [8] as well as Aziz *et al.* [60].

2.3.1.1 Ferricyanide/ferrocyanide

Several degradation reactions have been identified for ferrocyanide and are indicated in Table 4.

Table 4 Ferrocyanide degradation reactions

Reaction	Source
Degradation of ferri/ferrocyanide under light exposure	[61]

$$4\,\text{Fe}^{3+} + 3\,[\text{Fe}^{\text{II}}(\text{CN})_6]^{4-} \longrightarrow \text{Fe}^{\text{III}}[\text{Fe}^{\text{III}}\text{Fe}^{\text{II}}(\text{CN})_6]_3 \qquad [62]$$
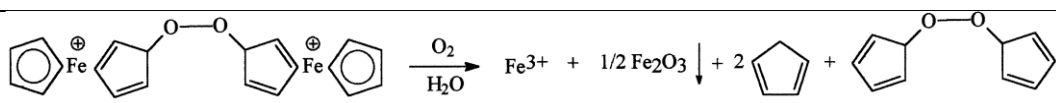
Formation of prussian blue upon exposure to the light in acidic media

Acid degradation of ferrocyanide [33]

Basic degradation of ferrocyanide [33]
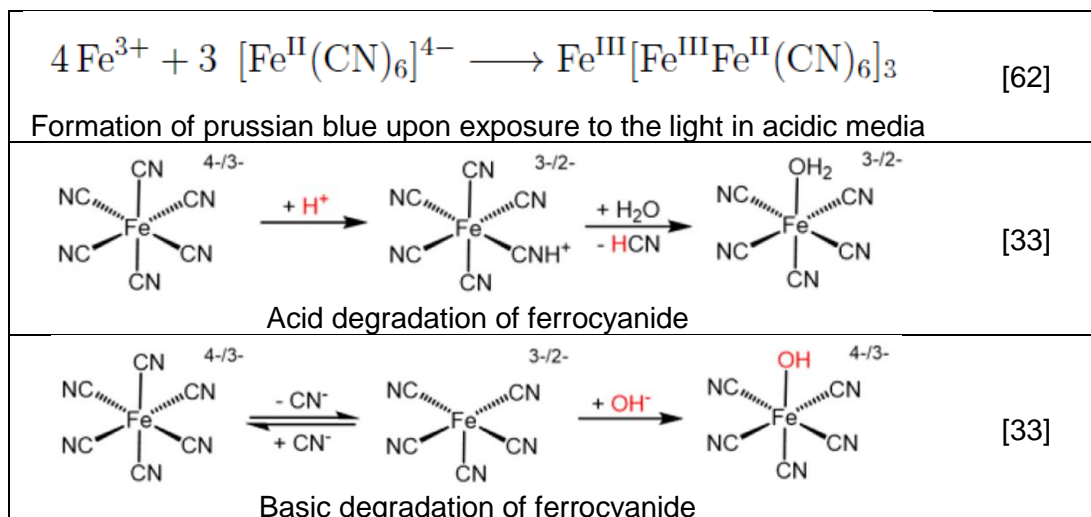
The ferricyanide and ferrocyanide are known to be light-sensitive, and their degradation under the light is pH-dependent [61]. The reaction scheme is shown in Table 4. The degradation rate is inversely proportional to the free cyanide concentration in solution. This rate thus is higher at the beginning and decreases over time [63]. Formation of Prussian Blue was also reported *in situ*, with the help of symmetric cell characterization [62,64,65]. It was detected on the membrane by FTIR-ATR analysis, after exposure to light in acidic conditions. The reaction scheme is proposed in Table 4. The formation of Prussian Blue is a consequence of the presence of Fe(III) species in solution. Ferrocyanide and ferricyanide species are also unstable under acidic conditions and generate toxic HCN as seen from *ex situ* studies, following the reaction scheme shown in Table 4 [66]. As in acidic environment, the reduced form is unstable in alkaline media, as suggest the results shown in Table 4 obtained *in situ* with half-cell configuration [33]. The conditions were the following: charge and discharge between -0.4/0.4 V, current densities from 40 to 100 mA/cm². The samples were studied after 300 cycles by ^{13}C NMR. Both decomposition products in acidic and alkaline media are different electroactive species. However, Ventosa *et al.* recently reassessed the stability of ferrocyanide in alkaline media, and said that ferrocyanide was not degraded as proposed before with the release of CN^- ion, but that the observed capacity fade was caused by OER [67].

2.3.1.2 Ferrocene

Table 5 Ferrocene degradation reactions

Reaction	Source
Decomposition of ferrocenium by oxygen in organic media in the presence of water	[68]
Decomposition of ferricenium by nucleophilic attack in organic media	[69]
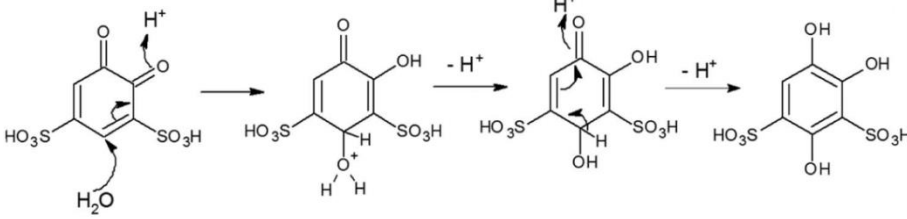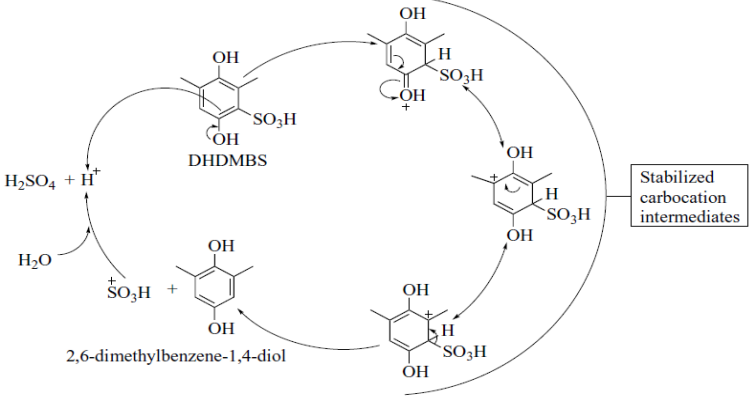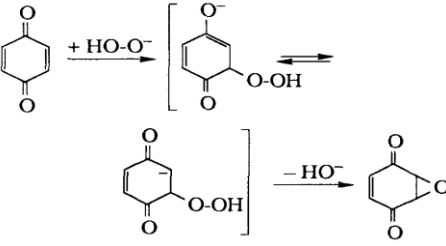
Dioxygen decomposition of ferrocenium in the presence of water was reported in acetonitrile [68]. The reaction scheme is exposed in Table 5. The products are identified *ex situ* by CV, FTIR, GC-MS and electrochemical quartz micro balance (EQCM). There is precipitation of iron oxide, and formation of Fe^{3+}, another electrochemically active species. Decomposition of ferricenium by nucleophilic attack in organic media, as represented in Table 5, was reported in acetone, nitromethane or acetonitrile *ex situ* [69]. The reaction forms ferrocenium and another iron complex. The products are identified with ESR and electronic

absorption and quantified via UV measurements. As far as we know, no decomposition reaction was proposed for ferrocene in aqueous media, suggesting a high stability of this component in the conditions encountered in AORFBs.

2.3.1.3 Quinone

The degradations paths have been more thoroughly explored for quinones than for other technologies. They are especially sensitive to nucleophilic additions or substitutions [70]. Main reactions are summarized in Table 6.

Table 6 Quinones degradation reactions

Reaction	Source
Michael addition on benzoquinones	[40]
Protodesulfonation of DHDMBS in acidic media	[71]
Epoxide formation in basic solution in the presence of H2O2	[72]

Disproportionation and dimerization of anthraquinones

Nucleophilic attack on susbstituted anthraquinones
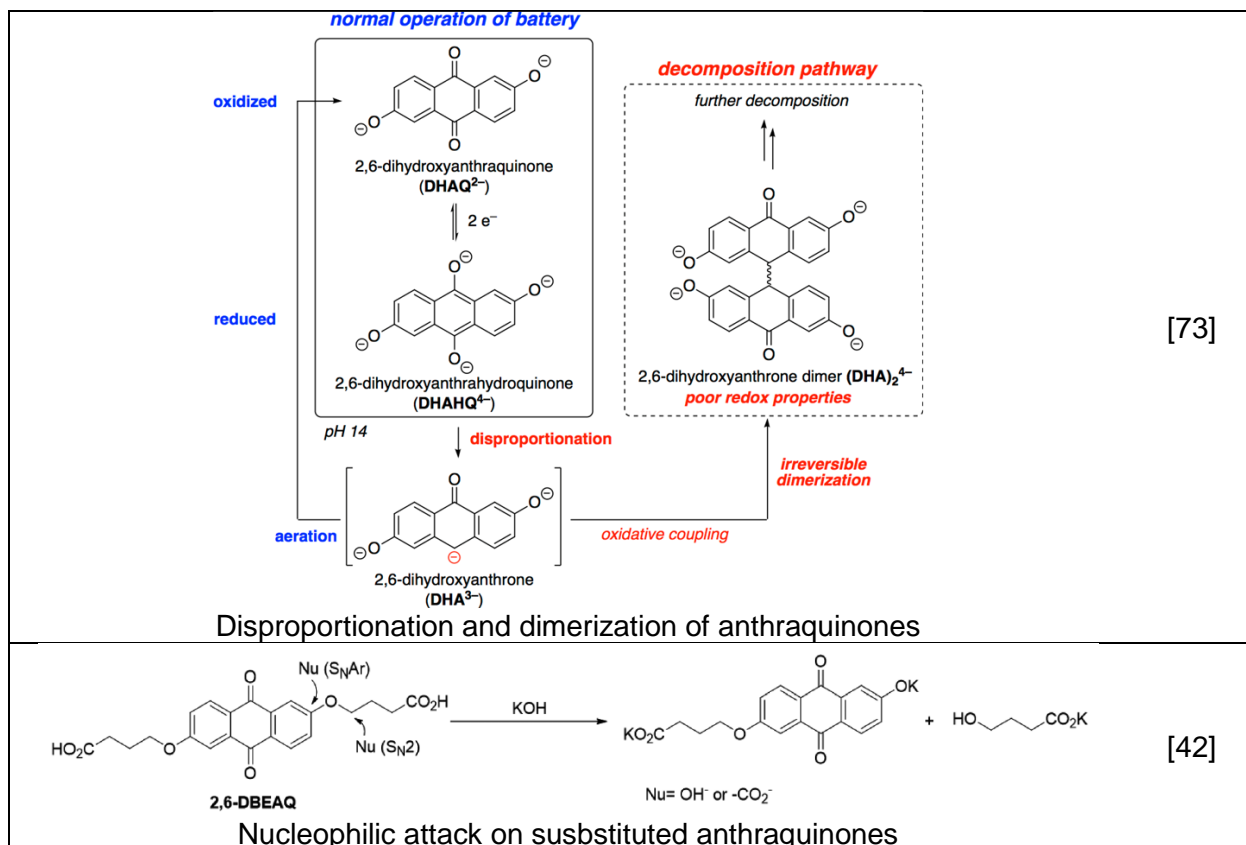
Tabor *et al.* did a computational study of quinones stability *vs.* their structure using DFT coupled with semi-empirical calculations [74]. They found that as their reduction potential – hence their electron deficiency or Lewis acidity – increased, the species became more sensitive to nucleophilic additions, with a breaking point above 0.9V vs. SHE [60]. Arguably the most well-known degradation of benzoquinones is a rapid nucleophilic attack in aqueous solution, known as Michael addition. This reaction, shown in Table 6, has been observed *ex situ* in several publications [40,75,76]. The reaction products were identified by ^{1}H NMR characterization experiments. The fully substituted benzoquinone formed is a redox active compound, but its potential is decreased of 100 mV for each added group, reducing the cell voltage. The multi-hydroxylated compounds often show less reversible redox behavior [77]. Furthermore, an excess amount of the other side material is required to fully convert the benzoquinone during the first stages of operation, resulting in excess active material unutilized further during charge and discharge. Incomplete utilization of this active material results in a reduced current density in the cell [40]. The authors thus designed a Michael addition-resistant molecule, dihydroxy dimethylbenzene sulfonic acid (DHDMBS) [75]. The strategy is to fully substitute the benzoquinone with methyl groups to avoid free sites for secondary reactions. A cell with AQDS and DHDMBS was cycled at 100 mA/cm², without capacity fade for 25 cycles. However, they started to notice capacity fade after further cycling. The DHDMBS resistant to Michael reaction is sensitive to another side reaction called "protodesulfonation" shown in Table 6, observed *in situ* under acidic conditions. This reaction is quite slow compared to Michael addition, but not negligible, the capacity fade rate being 0.23% per hour (pseudo-first-order rate constant determined at 1 M sulfuric acid is 2.10^{-6} s^{-1}). Reaction rate increases with temperature and pH decrease (a dark precipitate rapidly forms in 4 M sulfuric acid). The products of cycling were analyzed by ^{1}H-NMR, ^{13}C-NMR and Electrospray Ionization coupled with High resolution mass spectroscopy (ESI-HRMS) [71]. The formed 2,6-dimethylbenzene-1,4-diol is not very soluble in water, and precipitates when present with an excess of 10 – 15%. In mild basic solutions with the presence of H_2O_2, para-benzoquinone forms 2,3-epoxy-p-benzoquinone. The oxidation reaction by hydrogen peroxide shown in Table 6 has been observed ex situ, and is usually followed by nucleophilic attack [72]. The reaction products were identified by HPLC, GC-MS, NMR and UV spectroscopy. The epoxide is formed with a second order rate constant of 0.77 M^{-1}.s^{-1}.

Anthraquinone, although being more stable and less prone to crossover than benzoquinones (but more than naphthoquinones, which are more substituted), were also reported to degrade in certain conditions. Brushett *et al.* studied the evolution of 9,10-anthraquinone-2,7-disulfonic acid both in acidic and mildly alkaline media (pH 9.76) [78,79]. They found that the in both media, the anthraquinone is prone to dimerization, with dimerization equilibrium constants of 5 and 8 M^{-1} in acidic and alkaline media respectively. The dimer formed is electrochemically inactive, and its concentration can be reduced by increasing temperature even though it is still present. They found that during cell operation, the dimer tends to disappear in favor of an electrochemically active quinhydrone, and the equilibrium constant shifts in favor of the monomer [79]. Unsubstituted anthraquinone produced anthrone in highly acidic conditions [80]. Similarly, a 2,6-DHAQ/Fe(CN)$_6$ cell showed capacity fade of 5-8% per day at pH 14 [73]. DHAQ was cycled in a symmetric cell and decomposition products DHA (anthrone) and then (DHA)$_2$ were identified in alkaline anaerobic conditions using MS, ^{1}H-NMR and HPLC compared to a pristine sample. The dianthrone formed, despite still being redox-active, is impractical for a use in redox-flow batteries due to its higher potential and lower capacity. Furthermore, this product is unstable in strong alkaline conditions. However, the anthrone produced can be oxidized back to DHAQ by aeration, restoring the battery capacity. Another study uses online Electron Spin Resonance (EPR) and NMR to track the concentration of the radical intermediate DHAQ$^{3-\cdot}$ [81]. They revealed formation of both DHA and 2,6-dihydroxyanthranol (DHAL) during high SOC (1.6 or 1.7V) potential holds. The formation of such degradation products is concentration dependent, increasing with DHAQ concentration as DHAQ$^{3-\cdot}$ concentration decreases.

One strategy to mitigate the capacity fade is to limit the cutoff voltage in the cycling conditions. As anthrone is formed at high SOC of the battery (i.e. when the negolyte is in its fully reduced form), limiting the cycling window results in less anthrone formation, and can decrease the capacity decay from 5.6%/day at a cutoff of 1.6V to 0.14%/day at a cutoff of 1.25V. However, the accessed capacity decrease from 99.9% to 88% of the theoretical capacity in these conditions. Another strategy is to change the quinone used. 2,6-DBEAQ synthesized by Aziz et al. showed only slight degradation with 0.04% capacity fade per day at pH 14 [82]. However, ^{1}H RMN revealed that at higher temperature and even more in strong alkaline conditions, this species could undergo nucleophilic substitution as shown in Table 6 [42]. The cleavage of both sides of the anthraquinone leads back to 2,6-DHAQ. An increase in temperature and pH increases the degradation rate of DBEAQ, even though it remains low compared to other quinone degradations reactions. The results were obtained with half-cell experiments, and led to the synthesis of 2,6-DPPEAQ, more stable at pH 12.

2.3.1.4 TEMPO

Several degradations reactions have been identified for TEMPO and are indicated in Table 7.

Table 7 TEMPO degradation reactions

Reaction	Source
Disproportionation-dimerization of TEMPO molecules under acidic conditions	[8]

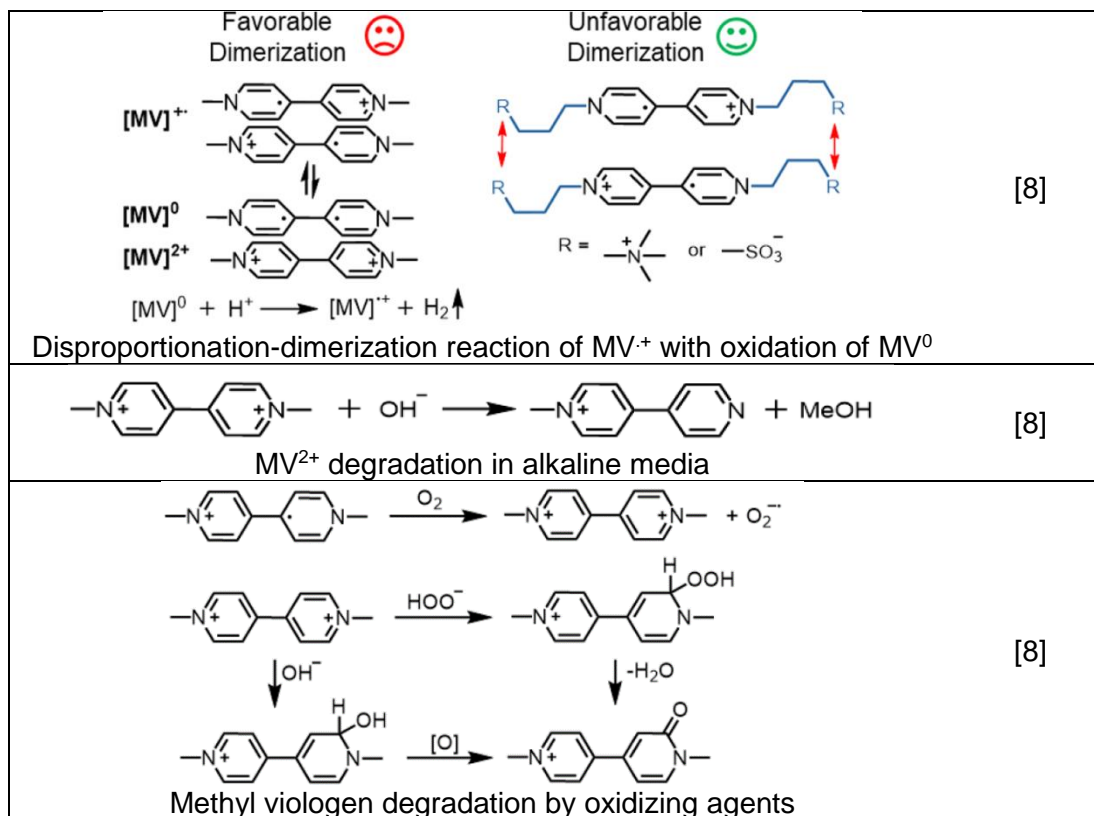|	
TEMPO-catalyzed alcohol oxidation	[8]
TEMPO decomposition in acidic or basic media with opening of the aromatic circle	[8]
Oxidation of TEMPOL to form TEMPONE	[83]
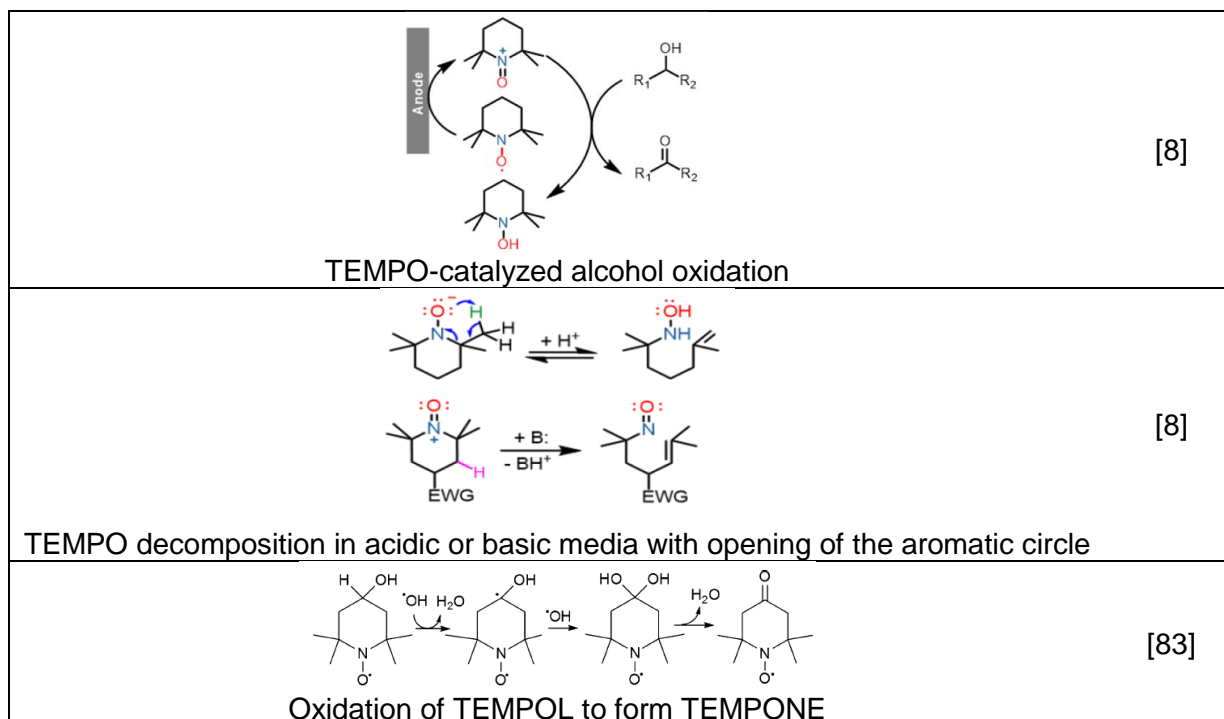
In warm acidic aqueous solutions, TEMPO disproportionate into its oxoammonium salt and a nitroxyl anion. The anion is then protonated into TEMPOH, an inactive redox species. The TEMPOH formed can then form a dimer with TEMPO free radicals, shifting further the equilibrium of dismutation. The reaction steps are presented in Table 7 [8]. TEMPO are known catalysts for alcohol oxidation [37]. The leading mechanism is presented in Table 7, where TEMPO forms here again TEMPOH. The reaction can happen between two molecules of 4-HO-TEMPO, for instance. This loss of active material has been described *ex situ* from battery operation. TEMPO can be subject to a decomposition with opening of the aromatic ring. This degradation mode has been reported *ex situ* both in acidic and in basic media [84,85]. This reaction, presented in Table 7, can be broadened to any TEMPO derivative with an electron withdrawing group in ortho-position of the N=O link. Another degradation mechanism reported for 4-HO-TEMPO (TEMPOL) is its self-oxidation with hydroxyl radicals, to form 4-oxo-TEMPO (TEMPONE) [83]. The scheme proposed by Marshall et *al.* is presented in Table 7. The reaction products and intermediates were observed by electron spin resonance spectroscopy (ESR) and ESI-MS. 4-oxo-TEMPO is another redox active species, with a slightly higher redox potential but lower solubilities of both oxidized and reduced form in water than 4-HO-TEMPO [86].

2.3.1.5 Viologen

Main identified viologen degradation reactions are indicated in Table 8.

Table 8 Viologen degradation reactions

Reaction	Source

Disproportionation-dimerization reaction of MV$^{.+}$ with oxidation of MV^0	[8]
MV^{2+} degradation in alkaline media	[8]
Methyl viologen degradation by oxidizing agents	[8]

The radical MV$^{+.}$ formed upon reduction of MV^{2+} is prone to dimerization, forming MV^0 and MV^{2+}. In addition to the imbalance caused by the disproportionation reaction, the MV^0 formed is insoluble in water and can precipitate or be oxidized by protons leading to H$_2$ evolution. Substituted viologens like (NPr)$_2$V or (SPr)$_2$V are less sensitive to dimerization thanks to the repulsion between the pendant groups, as shown in Table 8 [87]. This different stability behavior observed in flow cells was explored *ex situ*, by isolating the molecules in an argon filled glovebox with UV measurements. Another degradation of MV^{2+} reported *ex situ* is the reaction between hydroxide ions and viologen in basic solutions (pH > 12) [88]. The formed product, shown in Table 8, is electrochemically inactive. MV$^{+.}$ is oxygen sensitive and can be oxidized to MV^{2+} [8]. MV^{2+} also reacts with oxygen to form active oxygen species such as hydrogen peroxide, that can further react with viologen to cause its oxidation and deprotonation of the viologen ring, following the scheme in Table 8 [89]. These reactions have been observed *ex situ*, in the field of biochemistry, and form electrochemically inactive species.

2.4 Summary of the degradations

Table 9 sums up the major degradation mechanisms listed above for the electrodes and bipolar plates, the membrane, and the electrolyte. There is a detailed list of all the organic electroactive species families, with the corresponding aging phenomena as seen above. For each degradation, we propose a classification that is based on the corresponding microscopic physical phenomena as well as the effects expected on the performances of the battery (macroscopic) are detailed. Physical phenomena which happen at the microscopic scale are divided in four categories:

- Loss of active material (Loss$_{AM}$), which correspond to degradations of electroactive material in the posolyte or the negolyte, involving or not electrons. Loss of active material via an electrochemical reaction also produces unbalancing,
- Unbalancing of the electrolytes, which correspond to reactions or phenomena that utilize electrons – for example side reactions –, thus these electrons are not used in main reactions. It then induces charge unbalancing and a decrease in faradaic efficiency,
- Internal resistance increase (R ++), which regroups all the phenomena that contribute to an increase in the resistance of the battery,

- Pressure drop increase (Δp ++), which corresponds to an increase in pressure drop caused by a change in fluidics.

Macroscopic phenomena which can be measured are the following:

- CE loss, which is a result of unbalancing or loss of active material,
- Capacity fade, which also happens after unbalancing or loss of active material,
- EE loss, resulting from an increase in resistance or in pressure drop,
- Catastrophic failure, which here refers to a sudden failure forcing the interruption of battery operation, with no possibility to recover from this state without heavy maintenance.

Finally, diagnostic tools useful for analyzing degradations – both qualitatively and quantitatively – are listed. This classification is different from the one established by Aziz et al. in two distinct papers, that considered CE loss, capacity loss and apparent capacity fade [60,90]. In this table, we propose a classification of the effects on the performances considering both electrolytes in the battery are in stoichiometric equilibrium.

Table 9 Reported degradation mechanisms in the literature, along with their effects on performances and diagnostic tools

Component	Reported degradations	Microscopic	Macroscopic	Diagnostic tools
Electrodes & Bipolar plates	Thermal & Mechanical Chemical aging	R ↗ R ↗	EE loss EE loss	Visual inspection, EIS, XPS, Electrochemical techniques, SEM, MS
Membrane	Water transfer Chemical degrad. Mechanical degrad.	$Loss_{AM}$ R ↗ Δp & R ↗	Capacity & CE loss EE loss Catastrophic failure	Visual inspection, Spectroscopy, FTIR, SEM, ^{1}H NMR, Visual inspection
Electrolyte (general)	Leakage/clogging Precipitation Crossover Side reactions	Δp ↗ Δp ↗ & $Loss_{AM}$ Unbalancing & $Loss_{AM}$ Δp ↗ & unbalancing	Catastrophic failure Catastrophic failure Capacity & CE loss Capacity & CE loss	Visual examination, Spectroscopy, ^{1}H NMR,
Ferrocyanide	Photodegradation HCN formation (acidic) Degradation (basic)	$Loss_{AM}$ Unbalancing Unbalancing	Capacity & CE loss Capacity & CE loss Capacity & CE loss	CV, LSV, UV-vis spectro., IR spectro., ^{13}C NMR
Ferrocene	Decomposition in organic media	$Loss_{AM}$ & unbalancing	Capacity & CE loss	CV, LSV, FTIR, GC-MS, EQCM, ESR, UV-vis spectro.
Quinone	Nucleophilic attack Protodesulfonation Dimerization Anthrone formation	Unbalancing & $Loss_{AM}$	Capacity & CE loss	^{1}H NMR, ^{13}C NMR, UV-vis spectro., MS, HPLC, EPR

TEMPO	Disproportionation – dimerization	$Loss_{AM}$	Capacity & CE loss	CV, LSV, ^{1}H NMR, IR, UV-vis spectroscopy, ESR, ESI-MS
	Alcohol oxidation	$Loss_{AM}$	Capacity & CE loss	
	Ring opening	$Loss_{AM}$	Capacity & CE loss	
	Oxidation (basic)	Unbalancing	Capacity & CE loss	
Viologen	Dimerization Alkaline degradation Oxygen degradation	$Loss_{AM}$	Capacity & CE loss	UV-vis spectroscopy, CV, LSV, ^{1}H NMR, ^{13}C NMR

We can see that degradations of the electrodes or bipolar plates typically lead to EE loss, whereas degradations concerning the electrolyte and electroactive species mainly lead to capacity fade and CE loss. Capacity fade and CE loss occur typically when an electroactive species at the negolyte or the posolyte is transformed either in a non-electroactive specie or in a molecule with a sufficiently low solubility so that it precipitates, resulting in a loss of active material [60]. If the product is electrochemically active but its redox potential is different from the reactant's, it causes unbalancing between positive and negative sides of the battery, resulting in EE loss. If one side is capacity limiting, the conclusions may differ, as it is the case in the study by Aziz *et al.* of the quinone-bromide flow battery [90]. A change in the electrolyte flow – caused by precipitation, gas evolution or degradation of the electrode for example – causes a change in the pressure drop, leading to an increase of the global resistance and thus EE loss or, ultimately, catastrophic failure. Figure 2 presents a scheme for describing the main degradations taking place in an organic redox flow battery. Figure 3 is a summary of the performances' degradations and their proposed causes, making a link between macroscopic and microscopic scale.
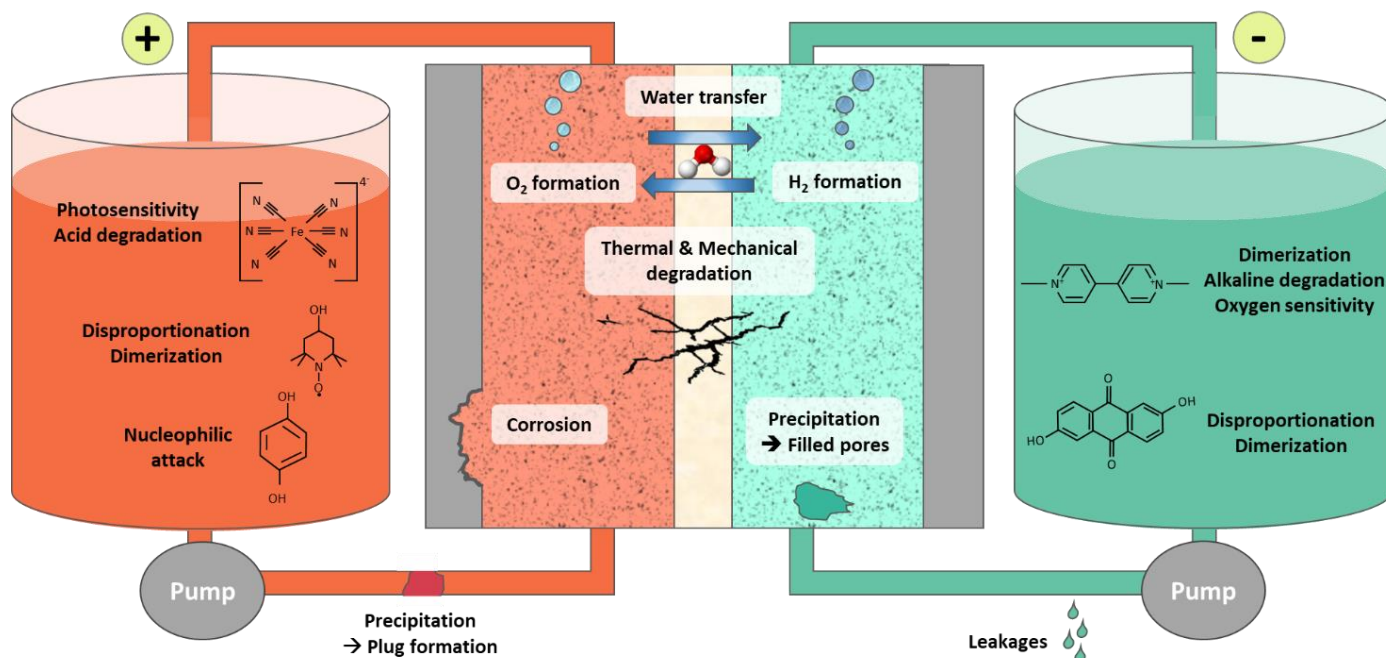

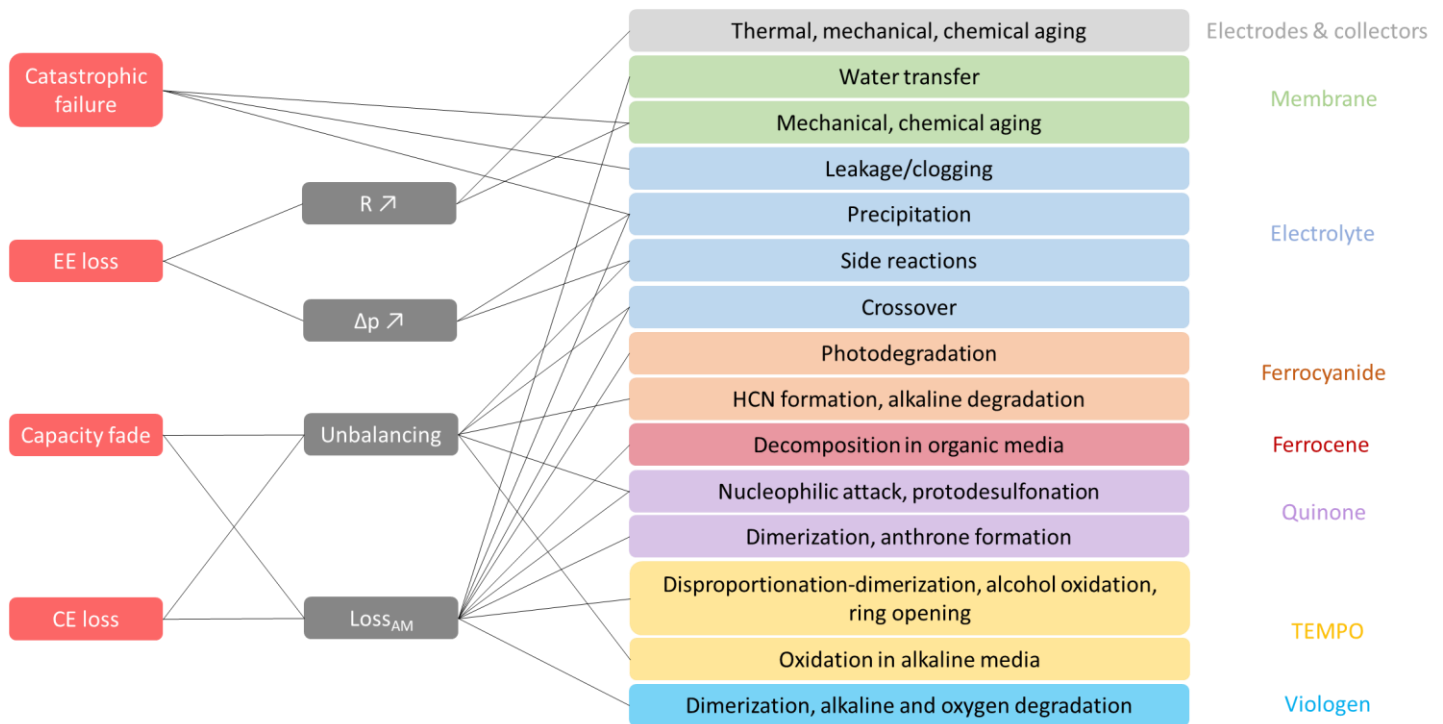**Figure 2 Main degradation mechanisms in organic redox flow batteries**

Figure 3 Performances' degradations and their causes in aqueous organic redox flow batteries

2.5 Experimental investigation of ORFB aging

Experimental data are crucial to determine RFB aging state, as was outlined in the comprehensive review by Mench *et al.* [91]. Electrochemical experiments are usually used in the first instance to assess the global performances of the battery and evaluate its level of aging. They mainly aim to determine the capacity of the battery, evolution of the battery resistance, loss of energy efficiency. Subsequently, physicochemical characterizations can be used to identify aging micro-phenomena. The latter characterizations are usually destructive and can give qualitative or quantitative results on degradation phenomena and products.

2.5.1 Performance evaluation methods

Different cell configurations are exploited to investigate degradations of the battery [10]. The cell can be either in flow mode or static. Static cell configuration can be used for initial stability tests, to detect major degradations, but is not suited to long-term analysis. In flow mode, the electroactive species are usually first tested in symmetric configuration, meaning that the same electrolyte is used on both sides of the membrane, thus eliminating crossover. If one side is in excess, it enables focusing on the degradations of the other side. Indeed, the capacity fade observed is then only related to degradations or side reactions of the limiting side. When the stability has been studied in symmetric cell configuration, the next step is to challenge the electrolyte performance in asymmetric configuration, with different electrolytes on both sides of the battery. Here again, the electrolytes can be in a first step unbalanced, with an electrolyte in excess to focus on the degradations of the other side, and to study the stability depending on the SOC of this capacity limiting side [60]. Finally, the last step is doing cycling tests made in charge-balanced asymmetric cell configuration, with a stoichiometry in the concentration of electrons accessible on both sides. This is the closest configuration to the reality of operation but complicates the understanding and decorrelation of each degradation. Accelerated stress tests are widely used for other electrochemical storage systems, such as PEM fuel cells and Li-ion batteries [50,92,93]. An original two cells-in-series setup was developed by Mench *et al.* to study degradations of the electrodes and the membrane in a vanadium redox flow battery, in which degradations occurred seven times faster than in normal conditions [94].

Charge-discharge curves are the most widely used method for basic characterization of RFBs performances. Cycling tests can be performed in two different ways: potentiostatic or galvanostatic-potentiostatic. In potentiostatic cycling (Constant voltage or CV), charge or discharge is performed with a constant voltage instruction [95]. In galvanostatic-potentiostatic cycling (Constant current-constant voltage or CC-CV), charge or discharge is performed with at a constant current until the limit voltage is reached, followed by a constant voltage phase until the current has decreased below a stated value, usually a 20th or a 50th of the total cell capacity [41]. In the latter method, the constant voltage step enables accessing total available capacity in the electrolyte. Pauses at various SOC between the cycles, also called Current Interruptions, can provide information on the influence of SOC on the degradations [96]. Polarization curves as well as power density curves are mainly used for fuel cells performance evaluation [9,97]. Polarization curves give the relationship between cell voltage and current density. Power measurements of a full cell can be performed by discharging the cell at various SOC and current densities. To evaluate the resistance of a redox flow battery, Electrochemical Impedance Spectroscopy (EIS) is a commonly used tool and the results' treatment and interpretation enable decoupling the different contributions to the global resistance. Hybrid pulse power characterization (HPPC) tests are widely used to determine internal resistance in lithium-ion batteries or other high-power systems, and can also be applied to evaluate redox flow battery resistance [98].

2.5.2 Degradation diagnostic methods

In order to determine if there is a change in the concentration of the electrochemical species or new electrochemical products, a common electrochemical method is cyclic voltammetry [91]. Electrochemical reaction mechanisms can be studied with Rotating Disk Electrode (RDE) voltammetry. When degradations of the performances are observed, the investigation of the degradation phenomena involved is made with the help of physical characterizations. The most used are spectroscopy techniques (UV-vis, IR, Raman) for assessing electrolyte stability and redox reaction reversibility, and microscopy analysis (Scanning electron microscopy, Transmission electron microscopy) to explore surface changes, for example on the membrane or the electrodes. NMR spectroscopy is widely used to study the evolution of electrolytes' composition. Mass spectroscopy is also used to detect new products in the electrolytes and can be coupled to chromatography techniques. XPS, X-ray tomographic microscopy (XTM) and XRD are commonly used to study electrode morphology degradations. Electron spin resonance (ESR) spectroscopy is used to study crossover and transport of water through the membrane in VRFBs [91].

Online measurements of the active species concentrations have been explored in certain cases. Tong *et al.* reported in situ UV-vis spectrophotometry for concentration monitoring in a quinone based redox flow battery [99]. Similarly, Schubert *et al.* developed an approach based on IR spectroscopy, which provides real time data concerning electrolyte SOH in a redox flow cell [100]. Zhao *et al.* used an online NMR setup for studying the degradations in redox flow batteries [101].

3 Redox flow batteries modelling and aging modelling

The modelling of a battery gives useful insights on performance prediction of the battery operation at different scales. Modelling has been thoroughly developed for different technologies such as Li-ion and PEMFC, and has been easily transposed, with minor changes, to vanadium redox flow batteries [102,103]. For instance, modelling the OCV and SoC of a redox flow cell is essentially the same as in a Li-ion battery, while the species transport in the fluid circuit, the porous electrodes and the membrane are modelled based on PEMFC models [104].

3.1 Empirical and physical models

The first models developed are empirical electrical equivalent circuits (EEC), which reproduce the behavior of cells with the help of electrical components [105–107]. The simplest form is with a RC circuit, and the circuit can be improved by adding resistances, capacitors, Warburg diffusion elements etc. The EEC models are parameterized with the help of EIS measurements, and they are very fast to compute, allowing the modelling of large timespans in decent computing time. These models describe the evolution of the resistance and capacity of the cell without making a link with the corresponding physical mechanisms.

Physical models are based on equations describing the behavior of the battery. They can accurately represent the physical reality of cell operation with some assumptions and are efficient to predict cell cycling behavior assuming that the degradation reactions are well represented. The accuracy and complexity of the chosen assumptions result in different computing times. The parameters' values used in the modelling are either defined in the literature, calculated experimentally or fitted, by trying to reproduce the tendency of experimental data [108]. The fitting of parameters is often far from being straightforward as the problems aren't linear and phenomena are coupled. Physics-based models mesh is also important: a 0D model considers no space variation of any parameters in each component, while 1D, 2D or 3D models take into account spatial variation along one, two or three dimensions [31,64,109,110]. Among these three last approaches, finer meshes lead to better accuracy but higher computing time. The highest complexity level models are ab-initio models, which exploit the first principles without additional assumptions. Ab-initio model can be used for exploring new tailored molecules, or predicting the solvation of molecules in different solvents [111–113].

The model complexity is chosen accordingly to the pursued objectives, the modelled scale, and the computation power. Indeed, building an EEC model on the material scale makes no sense as the information obtained and the accuracy would be irrelevant, as well as choosing a 3D model or ab initio model to represent the battery at the process scale: the computing time would be too large, and the level of details too fine.

Redox batteries can be modelled at different scales: materials, component, cell, stack, battery, or process. Some studies modelled only the organic redox molecules very precisely, in order to predict their physicochemical properties [35,114]. Many authors focused on only one component of the redox flow cell: the membrane and the porous electrodes being the most studied [115,116]. Several models exist for an entire redox flow cell [108,117]. Finally, the largest scale for models includes several cells in series or parallel, with the associated tanks and fluid circuit [118]. These different scales are dependent on each other: indeed, larger modelling scales require a certain quantity of data. This data is accessible from smaller scales modelling results.

3.2 Physical modelling of a redox flow cell

Physical models can be divided into several sub-models, the most common being electrochemical kinetics, transport models in porous electrodes as well as in membrane, fluid mechanics and electrical models. Some additional sub-models can be added, such as a heat transfer model to account for non-isothermal elements, or mechanical sub-models accounting for pumping power losses [108,119]. This section

describes a basic model for redox flow cells, with the generally used laws of physics for model building [120]. Physical phenomena are described by many parameters, detailed in Table 10. It is important to note that most of the existing redox flow battery physical models are for VRFBs. There are only a few models for organic flow batteries yet [121].

Table 10 Physical parameters for the physical description of a redox flow cell

Parameter	Description
a_s (m^{-1})	Specific area
α_k	Transfer coefficient for reaction k
F (C.mol^{-1})	Faraday constant
k_k (m.s^{-1})	Kinetic constant for reaction k
a_o (mol.m^{-3})	Oxidant bulk activity
a_R (mol.m^{-3})	Reductor bulk activity
c_o (mol.m^{-3})	Oxidant bulk concentration
c_R (mol.m^{-3})	Reductor bulk concentration
c^s (mol.m^{-3})	Surface concentration
R (J.mol^{-1}.K^{-1})	Gas constant
T (K)	Temperature
η_k (V)	Overpotential for reaction k
ϕ_s (V)	Solid phase potential
ϕ_e (V)	Electrolyte (liquid) phase potential
E_0' (V)	Standard potential
E_0^k (V)	Equilibrium potential for reaction k
k_m (m.s^{-1})	Mass transfer coefficient
D_i (m².s^{-1})	Diffusion coefficient for species i
D_i^{eff} (m².s^{-1})	Effective diffusion coefficient for species i
N_i (mol.m^{-2}.s^{-1})	Flux of species i
S_i	Source term for species i
n_i	Stoichiometry of species i
c_i (mol.m^{-3})	Concentration of species i
d_f (m)	Pore size of the porous electrodes
K_{CK}	Kozeny-Carman constant
μ (Pa.s)	Dynamic viscosity of the electrolyte
μ_{H2O} (Pa.s)	Dynamic viscosity of water
ε	Porosity of the carbon felt
p (Pa)	Pressure
v_e (m.s^{-1})	Electrolyte velocity in porous electrodes
v_e^m (m.s^{-1})	Electrolyte velocity in the membrane
k_p (m²)	Hydraulic permeability
k_ϕ (m²)	Electrokinetic permeability
c_c^e (mol.m^{-3})	Cations concentration in the electrolyte
c_c^m (mol.m^{-3})	Cations concentration in the membrane
κ^{eff} (S.m^{-1})	Effective conductivity of the electrolyte
σ_s (S.m^{-1})	Electronic conductivity of porous electrodes
σ_s^{eff} (S.m^{-1})	Effective conductivity of porous electrodes
σ_{coll} (S.m^{-1})	Electronic conductivity of current collectors
R_e	Reynolds Number
ρ	Electrolyte density
d_p (m)	Diameter of the pipe
L_p (m)	Length of the pipe
z (m)	Height of the pipe
g (m.s^{-2})	Gravity acceleration

3.2.1 Reaction kinetics

Equations of the reaction kinetics are gathered in Table 11, k quoting the reaction type. For the electrochemical description of a cell, the typically used law for operating reactions is Butler-Volmer, presented in Equation 5. This relation is chosen because reaction kinetics are good, reactions are considered reversible and the precise steps of the reactions are not known [31]. The extended form of Butler-Volmer with the surface and bulk concentrations enables considering the mass transfer from the bulk to the electrode surface. Overpotential of the reaction is calculated thanks to the potentials' values in the solid phase and in the electrolyte. Standard potential of the reaction k is obtained with Nernst law. Surface concentration of reactants can be obtained via solving the two equilibria between mass transfer at the surface of the porous electrodes and the Butler-Volmer equation, shown in Equation 9 and Equation 10 [122]. The mass transfer coefficient k_m can be expressed as the ratio between diffusivity of the species considered D_i and pore size d_p in the carbon felt [123]. Mass transport is thus encouraged with a good diffusivity, or tightened pores.

Table 11 Equations describing reaction kinetics in redox flow cells

$$\nabla . i_e = a_s i_0^k \left[\frac{c_R^s}{c_R} \exp\left(\frac{\alpha_k F \eta_k}{RT} \right) - \frac{c_O^s}{c_O} \exp\left(-\frac{(1-\alpha_k)F\eta_k}{RT} \right) \right]$$	Equation 5
$$i_0^k = F k_k c_R^{\alpha_k} c_O^{1-\alpha_k}$$	Equation 6
$$\eta_k = \phi_s - \phi_e - E_0^k$$	Equation 7
$$E_0^k = E_0' + \frac{RT}{F} log\left(\frac{a_O}{a_R} \right)$$	Equation 8
$$k_m(c_O^s - c_O) = k_k c_R^{\alpha_k} c_O^{1-\alpha_k} \left[\frac{c_R^s}{c_R} \exp\left(\frac{\alpha_k F \eta_k}{RT} \right) - \frac{c_O^s}{c_O} \exp\left(-\frac{(1-\alpha_k)F\eta_k}{RT} \right) \right]$$	Equation 9
$$k_m(c_R^s - c_R) = -k_k c_R^{\alpha_k} c_O^{1-\alpha_k} \left[\frac{c_R^s}{c_R} \exp\left(\frac{\alpha_k F \eta_k}{RT} \right) - \frac{c_O^s}{c_O} \exp\left(-\frac{(1-\alpha_k)F\eta_k}{RT} \right) \right]$$	Equation 10

3.2.2 Mass transport of species in carbon felts

Equations representing the mass transport of species in the electrodes are presented in Table 12. The variation of the velocity in a porous medium is usually represented by Darcy's law, with a Kozeny-Carman law for representing the hydraulic conductivity as shown in Equation 11 [31,116,121]. A mass equilibrium on each species i in the liquid phase gives the Equation 12. S_i is the source term, representing the changes in species concentration thanks to reactions at the electrode. In the porous electrodes, the concentration fluxes $\vec{N}_i$ take into account transport by diffusion, migration and convection of every species in the cell (Equation 13) [31]. D_i^{eff} (m².s^{-1}) is the effective diffusion coefficient of the species i, corrected from the porosity of the electrode by a Bruggemann relationship such as shown in Equation 14 [124].

Table 12 Equations describing transport in carbon felts

$$\vec{v_e} = -\frac{d_f^2}{\mu K_{CK}} \frac{\varepsilon^3}{(1-\varepsilon)^2} \nabla p$$	Equation 11
$$\frac{\partial}{\partial t} \varepsilon c_i + \nabla \vec{N}_i = -S_i$$	Equation 12
$$\vec{N}_i = -D_i^{eff} \nabla c_i - \frac{n_i c_i D_i^{eff}}{RT} F \nabla \phi_s + \vec{v_e} c_i$$	Equation 13

$$D_i^{eff} = \varepsilon^{3/2} D_i$$	Equation 14

3.2.3 Transport in the membrane

The membrane is considered as flooded since liquid electrolyte is permanently flowing by and through it. The model developed by Bernardi and Verbrugge is used [125]. Equation 15 gives the fluid velocity in the membrane (Schlögl's equation) for a standard case with a cation exchange membrane, where water and protons only can cross the membrane. The membrane is not locally neutral but can be considered as globally neutral when considering the fixed species on the membrane (e.g. sulfonic acid groups for Nafion®). When considering only the movement of protons as charged species in the membrane, the current density satisfies Equation 16. At the membrane/electrolyte interface, current and species fluxes are continuous, whereas potential and concentrations of species are discontinuous due to the repulsion/attraction of the ions by the fixed charges of the membrane. A Donnan potential is commonly considered, to predict the relationship between concentration and potential jumps at the interface [126].

Table 13 Equations describing transport in the membrane

$$\overrightarrow{v_e^m} = -Fc_{H^+} \frac{k_\phi}{\mu_{H_2O}} \nabla\phi - \frac{k_p}{\mu_{H_2O}} \nabla p$$	Equation 15
$$\nabla\vec{\imath} = \nabla\overrightarrow{N_{H^+}} = -\frac{F^2}{RT} D_{H^+}^{eff} c_{H^+} \nabla^2\phi = 0$$	Equation 16
$$\Delta\phi = \frac{RT}{F} \ln\left(\frac{c_c^e}{c_c^m}\right)$$	Equation 17

3.2.4 Transport in pipes

Table 14 presents equations for describing electrolyte flow through the pipes [24,118]. Reynolds number is used to describe the flow regime. The pressure drop in pipes, valves and tanks is described by Equation 19, taking into account the friction losses h_f (m) and the minor losses h_m (m) due to valves, elbows, tanks etc. These losses are expressed by Equation 20 and Equation 21, respectively. The value of the loss coefficient $k_{L,i}$ depends on the geometry of the obstacle – elbow or bend, valve, transition from pipe to reservoir or reservoir to pipe – and is comprised between 0.04 and 1, as described in the literature [24,127].

Table 14 Equations describing transport in pipes

$$R_e = \frac{\rho v_e d_p}{\mu}$$	Equation 18
$$\Delta p_{pipes} = -\rho g\left(\frac{\Delta v_e^2}{2g} + \Delta z + h_f + h_m\right)$$	Equation 19
$$h_{f,i} = \frac{64}{Re_i} \frac{L_p}{d_p} \frac{v_{e,i}^2}{2g}$$	Equation 20
$$h_{m,i} = k_{L,i} \frac{v_{e,i}^2}{2g}$$	Equation 21

3.2.5 Electrical phenomena

Electrical phenomena happening in the current collectors, the electrodes, and the electrolyte as well as their relationships are expressed by equations in Table 15. The electrolyte is globally neutral, and the charge conservation principle is applied (Equation 22). In the electrodes (Equation 23) and in the electrolyte (Equation 25), charge conservation is expressed by Ohm's law. Electronic conductivity is corrected to account for the porosity of the material (**Erreur ! Source du renvoi introuvable.**). Electronic potential variation in the electrodes and in the current collectors are described by Equation 28 and Equation 30 respectively, in isothermal conditions.

Table 15 Equations describing electrical phenomena in the electrodes and the electrolyte

$$\sum_i n_i c_i = 0$$	Equation 22
$$i_s = -\sigma_s^{eff} \nabla \phi_s$$	Equation 23
$$\sigma_s^{eff} = (1-\varepsilon)^{3/2} \sigma_s$$	Equation 24
$$i_e = -\kappa^{eff} \nabla \phi_e - F \sum_i n_i D_i^{eff} \nabla c_i$$	Equation 25
$$\kappa^{eff} = \frac{F^2}{RT} \sum_i n_i^2 D_i^{eff} c_i$$	Equation 26
$$\nabla . \vec{\iota_s} + \nabla . \vec{\iota_e} = 0$$	Equation 27
$$-\sigma_s^{eff} \nabla^2 \psi = -\nabla . \vec{\iota_s}$$	Equation 28
$$-\sigma_{coll} \nabla^2 \psi = 0$$	Equation 29

3.3 Modelling the degradation mechanisms

Only few works are available in the literature regarding the modelling of the degradations in redox flow batteries. They mainly focused on either membrane and electrodes degradations crossover, parasitic side reactions involving vanadium species and hydrogen or oxygen gas formation, temperature changes during VRFB operation or mechanical losses related to pumping [50,104,119,122,128]. Degradations of the organic electroactive material in ORFBs and their modelling is still at an early stage, and some clues for the modelling could be obtained from the modelling of lithium-ion batteries degradations [129]. Overall, ORFB aging modelling potentially has a lot in common with models for PEMFC and lithium-ion battery aging [130].

3.3.1 Electrode degradations modelling

Degradations of the porous carbon electrodes in the presence of oxygen were modelled in PEMFC [50]. Carbon surface oxides are formed which are then oxidized in the presence of Pt. These models are interesting for redox flow batteries, even though they tend to focus on the degradation of the catalyst layer which is predominant and of greater importance for fuel cell performance, but not for RFBs. Corrosion current evolution in a vanadium flow battery was integrated in a multi-physics model by Merei et al. [119].

Mechanical degradations inducing a decreased active surface area or a change in the carbon felts porosity can be modelled by a modification of a_s and ε in reaction kinetics, mass transport and electrical equations.

3.3.2 Crossover modelling

Skyllas-Kazacos developed a simple kinetic model considering the transfer through the membrane by diffusion of vanadium ions only, with different mass transfer constants for each [131]. This model also considers the chemical side reactions resulting from crossover of vanadium species, which are assumed to be instantaneous. Their study indicated that this diffusion-only transfer resulted in an accumulation of vanadium ions in the positive half-cell, needing a rebalancing of electrolytes. Water transport through the membrane was described and modelled by Oh *et al.* [58]. Agar *et al.* modelled the crossover of vanadium ions by diffusion, convection and migration as described in Equation 30, as well as water transport through the membrane in a redox flow cell, in a 2D model [116] and then a 0D lumped-parameter model [132]. Table 16 presents the set of equations implemented to model crossover of multiple ions through the membrane in the 0D model developed by Agar and coworkers [132]. In the expression of the flux of species *i* through the membrane, the superscript *m* stands for the expression in the membrane, and the diffusion

distance $\delta_{diff} = t_{mem} + 2\delta_{BL}$ is composed of the membrane thickness t_{mem} and both diffusion layers δ_{BL}, at the positive and negative sides of the membrane. Fluid velocity in the membrane v_e^m is calculated from an alternate form of Schlögl's equation, shown in Equation 31. In comparison with Equation 15, to the first term on the right side of the expression is added a contribution from the electro-osmotic convection. The effective diffusion gradient $\nabla\phi_{diff}^m$ is calculated according to Equation 32, with the updated effective conductivity of the membrane given by Equation 33.

Table 16 Equations modelling the crossover

$N_i^m = -D_i^m \dfrac{(c_{i,neg}^m - c_{i,pos}^m)}{\delta_{diff}} - \dfrac{n_i c_i D_i^m}{RT} F \dfrac{(\phi_{neg}^m - \phi_{pos}^m)}{\delta_{diff}} + v^m c_i$	Equation 30
$v_e^m = -Fc_f \dfrac{k_\phi}{\mu_{H_2O}}(\phi_{neg}^m - \phi_{pos}^m + \nabla\phi_{diff}^m) - \dfrac{k_p}{\mu_{H_2O}}(p_{neg} - p_{pos})$	Equation 31
$\nabla\phi_{diff}^m = \displaystyle\sum_i n_i D_i^m (c_{i,neg}^m - c_{i,pos}^m)$	Equation 32
$\sigma_{eff}^m = \dfrac{F^2}{RT}\displaystyle\sum_i n_i^2 D_i^m c_i^m$	Equation 33

Boundary conditions were set according to the conservation of fluxes and currents at the electrolyte/membrane interfaces. 2D and 0D models were validated by comparing the simulated charge/discharge voltage as well as capacity fade with experimental data for a 45 cycles operation. Their 2D simulation results suggested that crossover of vanadium occurred from positive to negative side of the cell, and the resulting unbalancing led to capacity fade but had no significant effect on the cell efficiencies [116]. The vanadium transfer direction is the opposite from the results simulated by Skyllas-Kazacos *et al.* [131], which might be due to the fact that their study only includes diffusion and not also convection and migration transfer, and the operating conditions are different between the two studies. This difference underlines the importance of operating conditions and electrolyte transport properties (e.g. flow rate, viscosity).

With their reduced 0D model, they simulated longer cycling (1000 cycles) thanks to the reduced computing time [132]. They used the results to investigate the impact of the membrane thickness on the cell capacity fade and energy efficiency and concluded that compromises had to be made between these two parameters. With a medium-thick membrane, they observed an asymptote in the capacity fade, indicating the reaching of an equilibrium in the species concentrations after crossover. The crossover was largely dominated by diffusion in their simulation conditions.

In the case of aqueous organic flow batteries, crossover usually plays a less important role in the overall degradation phenomena because of the size of the organic molecules at stake. For that reason, crossover is not considered in most of the existing organic flow batteries models [121,133]. Recently, Kwabi *et al.* considered crossover in a 0D electrochemical model for a symmetric organic flow cell [134].

3.3.3 Side reactions modelling

Vanadium side reactions have been included in physical models of vanadium flow batteries by Skyllas-Kazacos *et al.* in 2012 [131], and taken up by Agar *et al.* in their crossover models [116,132]. They made the hypothesis of instantaneous redox reactions between V(II)/V(III) and V(V) after crossover of negolyte species into the positive side of the cell, and between V(IV)/V(V) and V(II) in the case of crossover of posolyte species into the negative side of the cell.

Water splitting are typical side reactions in aqueous redox flow batteries. H_2 and O_2 evolution have been included into some models, sometimes associated with the formation of gas bubbles and their impact on transport of the electrolyte [104,128,133,135,136]. Nernst potential for these secondary reactions (in

alkaline media) are calculated thanks to reactions' Equation 3 and Equation 4. The current arising from HER and OER is calculated with a Tafel kinetic representation, chosen because of the non-reversibility of the reaction [133]. The coefficient $\beta^{OER/HER}$ is the Tafel slope of the reaction. When formation of oxygen and hydrogen occurs, the liquid phase of the electrolyte is in equilibrium with a gas phase (gaseous O_2 or H_2). The following equations contribute to describe the multiphase mixture model [104,128]. These equations are presented in Table 17.

Table 17 Equations describing hydrogen or oxygen evolution reaction and their impact on the initial model

$$E_0^{OER/HER} = E_0^{\prime,OER/HER} + \frac{RT}{n_{OH^-}F} log\left(\frac{a_O}{a_R}\right)$$	Equation 34
$$j_f^{OER/HER} = i_0^{OER/HER} \exp\left(\beta^{OER/HER}\left(\Delta\phi - E_0^{OER/HER}\right)\right)$$	Equation 35
$$\alpha_l + \alpha_g = 1$$	Equation 36
$$\vec{v_e} = -\frac{d_f^2}{\mu K_{CK}}\frac{\varepsilon^3(1-\alpha_g)^3}{(1-\varepsilon(1-\alpha_g))^2}\nabla p$$	Equation 37
$$\vec{v_{slip}} = \vec{v_g} - \vec{v_e}$$	Equation 38
$$\vec{v_{slip}} = \frac{d_b^2}{\mu}\nabla p$$	Equation 39
$$\varepsilon\rho_g\frac{\partial\alpha_g}{\partial t} + \varepsilon\rho_g\nabla.(\alpha_g\vec{v_g}) = -S_g$$	Equation 40

Here α_l and α_g represent the volume fractions of liquid and gas, ρ_g (kg.dm^{-3}) the gas density, v_g (m.s^{-1}) the velocity of the gas bubbles, v_{slip} (m.s^{-1}) the slip velocity which is the relative velocity of the bubbles compared to the fluid, and S_g is the source term for creation of the bubbles – rate of H_2 or O_2 evolution in this case. The rest of the equations in the model stay the same, taking into account that the fraction of liquid is not 1 anymore in mass conservation equations (Equation 12 to Equation 14).

In their studies of oxygen [128] and hydrogen [104] evolution reactions in vanadium redox flow batteries, Al-Fetlawi *et al.* investigated mechanisms for bubble formation and how they affect the electrolyte flow. They focused on the influence of electrolyte flow rate, bubble diameter and operating temperature on OER, and the influence of flow rate, bubble diameter and current on HER. In both cases, bubbles formation reduces the active surface area of the carbon felts, as well as the effective diffusion coefficient of vanadium species by modifying the electrolyte flow. The impact is stronger for OER than HER because the volume of formed oxygen is greater than that of formed hydrogen in applied conditions. Increasing flow rate decreases gas volume fraction in the electrodes, thanks to the greater convection that removes bubbles from electrodes. As bubble diameter increases, slip velocity increases and gas volume fraction decreases because gas bubbles are removed quicker. OER reaction rate increases exponentially with temperature, thus provoking a decrease in current efficiency. An increasing applied current produces an increase in HER reaction rate, which can be balanced by increasing the electrolyte flow rate.

These simulation results are important since they give insights on how to manage hydrogen or oxygen generation by playing with operating parameters. However, they are limited to acidic electrolytes with vanadium active species. Cacciuttolo *et al.* developed an aqueous organic flow battery 0D model, which includes oxygen and hydrogen evolution reactions in alkaline media [133]. The model was validated on 2,6-DHAQ/Fe(CN)$_6$$^{4-}$ dissolved in KOH. The model does not include crossover of active species since the considered species are less prone to crossover through usual Nafion® membrane because of steric hindrance and their negative charge. Water splitting reactions are added to the electrochemical model with Tafel slopes. Their results show that oxygen evolution significantly impacts the performances of the

battery, while hydrogen evolution does not in considered experimental conditions, due to the poor catalytic activity of the carbon felt for hydrogen generation. The authors focused their study on different voltage limits U_{min} and U_{max}, since water oxidation and reduction current densities grow larger as we approach the voltage limits. Their conclusions underlined that energy increase is correlated to U_{min} increase, and that U_{max} plays a significant role on capacity, whereas U_{min} does not. Energy retention does not vary significantly with U_{min} or U_{max}, whereas energy efficiency decreases when the voltage window is enlarged. In studied conditions, positive-side main reaction competes with OER if cell voltage exceeds 1.6V. Similar approaches in neutral and acidic conditions would be interesting to have a wider perspective on the impact of HER and OER on aqueous organic flow batteries operation.

3.3.4 Electroactive species degradations modelling

Kwabi and Modak developed and validated an electrochemical model for a symmetric aqueous organic flow cell including some active reactant degradations [134]. They modelled, for instance, the rate of reactant decay R_{decay} (mol.L^{-1}.s^{-1}) of species A by a first order chemical degradation:

$$R_{decay} = \frac{d[A]}{dt} = -k[A]^b$$

k (s^{-1}) is the first order reaction constant and b is the decay reaction order. Diffusion-driven crossover can be modelled in the same way. As this mechanism is SOC-dependent, the authors studied the influence of the cycling protocol on the evolution of the capacity fade rate. They evidenced that the capacity fade rate is strongly correlated with the degradations mechanism but also with the cycling protocol (CC, CV or CCCV cycling, symmetrical or asymmetrical voltage limits, etc.). Their model can be adapted to several cycling conditions as well as to different supposed degradations paths.

Electroactive species degradation reactions have also been widely modelled for other battery technologies, such as lithium-ion [137]. If the effect of the degradation on the overall cell performance – in terms of CE loss, EE loss or capacity fade – can be assessed, then the modelling of the phenomena and their impact becomes easier. A hypothesis to classify the degradations happening to electroactive species is the one that we saw in section 2.4, which correlates the macroscopic effect on the cell performance and the microscopic phenomena occurring – loss of active material, unbalancing of the electrolytes or pressure drop increase –. Such microscopic phenomena can be incorporated in physics-based models by adjusting the species concentrations (active material loss), velocity of the fluid (pressure drop increase) [119], the redox potentials (unbalancing) etc. This modelling scheme is inspired from similarities between these electroactive material transformations and the ones taking place in lithium-ion batteries, giving namely loss of lithium inventory, positive or negative electrode material loss [129].

Modelling of some degradation schemes are proposed below:

- Precipitation of electroactive species can be modelled with a decrease in the species concentration (Loss$_{AM}$) and a change in the local pressure (Δp ↗). It can also lead to failure, represented by the end of the battery operation,
- Reversible electrochemical reaction towards a new electroactive couple can be modelled with a new current density via Butler-Volmer inducing a decrease in the reactant concentration and the energy efficiency, while the potential for this reaction is modelled with Nernst law. However, new reaction rate constants, transfer coefficients etc. render this modelling cumbersome. Another difficulty in modelling formation of new redox couples is predicting the current share between main reactions and new redox reactions, as well as anticipating for further degradations of new formed active species,
- Non-reversible electrochemical reaction – gas, insoluble product, or non-electroactive species formation for example – can be modelled with a new current density via Tafel producing a decrease in the reactant concentration and in current efficiency.

4 Conclusions

Redox flow batteries are an efficient way to store electrical energy under its chemical form. The architecture of the battery enables to decouple energy from power, allowing for good versatility along with safety of operation. Inorganic redox flow batteries, which have been developed for the past 50 years, are gradually giving way to organic electroactive materials. The properties of those can be efficiently tuned via functionalization, and they are potentially cheaper and less harmful for the environment. The main families of electroactive species were presented, with a discussion about advantages and drawbacks of each. The performances are promising but still far from reaching those of inorganic based (vanadium mostly), due to the difference in maturity between the technologies.

Degradations occurring on the cell physical components such as membrane or electrodes for vanadium redox flow batteries as well as side reactions are quite well reported in the literature and transcribe well to organic flow batteries. Degradations of the organic electroactive materials are, on the other hand, not thoroughly understood and there are only a few papers taking interest in describing the degradation reactions. Some of these degradation schemes were found to take place during battery operation and lead to a decrease in capacity fade, in coulombic and/or energy efficiency or a catastrophic failure. Summary schemes of the degradations reported for each component of an organic flow battery are provided in section 2.4.

Models of different nature are a great and promising way to replicate physical phenomena, enabling to make very long simulations in short periods of time and ultimately predicting the future life of the battery. The models can be empirical, meaning they are not based on any physical equations, semi-empirical or physical. The latter are based on physical equations describing the behavior of a battery, such as electrochemical, mass transfer or electrical equations. One of the main challenges is to model the degradation phenomena taking place during an organic redox flow battery cycling. A way to model the degradations, taking inspiration from other works on vanadium redox flow batteries, fuel cells and lithium-ion batteries aging, is to start from how they affect the battery performances and to classify them into "macro-mechanisms", that can be modelled in a similar fashion [129]. Examples of degradations modelling existing in the literature have been presented (crossover, side reactions, chemical degradation of active species), highlighting the existing work and other degradations mechanisms that have not been added to physical models yet.

The State of Health (SOH) is, as far as we know, not universally defined for redox flow batteries. For lead-acid and lithium-ion cells, SOH_{energy} and SOH_{power} are calculated looking at the ratio between actual and pristine discharge capacity and between the evolution of the resistance [138,139]. The SOH of a fuel cell can be defined with the evolution of its internal resistance. It is usually assessed with the help of non-intrusive methods, such as electrochemical impedance spectroscopy (EIS) diagrams or polarization curves [140,141]. Today, the health of a redox flow battery is mainly estimated by looking at the capacity fade. A more complete definition of the SOH – either global SOH or different SOH integrating ratios of parameters such as internal resistance, efficiencies, concentrations of active species, power, etc. – would enable a more standardized comparison of redox flow battery performances in the literature.

5 References

[1] IEA, World Energy Outlook 2020, Paris, 2020.

[2] B. Dunn, H. Kamath, J.-M. Tarascon, Science 334 (2011) 928–935. https://doi.org/10.1126/science.1212741.

[3] Z. Yang, J. Zhang, Kintner-Meyer, Michael C W, X. Lu, D. Choi, J.P. Lemmon, J. Liu, Chemical reviews 111 (2011) 3577–3613. https://doi.org/10.1021/cr100290v.

[4] R.H. Byrne, T.A. Nguyen, D.A. Copp, B.R. Chalamala, I. Gyuk, IEEE Access 6 (2018) 13231–13260. https://doi.org/10.1109/ACCESS.2017.2741578.

[5] P. Leung, X. Li, C. Ponce de Leon, L. Berlouis, C. Low, F.C. Walsh, RSC Adv. 2 (2012) 10125–10156. https://doi.org/10.1039/C2RA21342G.

[6] D.M. Kabtamu, J.-Y. Chen, Y.-C. Chang, C.-H. Wang, J. Power Sources 341 (2017) 270–279. https://doi.org/10.1016/j.jpowsour.2016.12.004.

[7] Y. Shi, C. Eze, B. Xiong, W. He, H. Zhang, T.M. Lim, A. Ukil, J. Zhao, Applied Energy 238 (2019) 202–224. https://doi.org/10.1016/j.apenergy.2018.12.087.

[8] J. Luo, B. Hu, M. Hu, Y. Zhao, T.L. Liu, ACS Energy Lett. 4 (2019) 2220–2240. https://doi.org/10.1021/acsenergylett.9b01332.

[9] Q. Zheng, F. Xing, X. Li, T. Liu, Q. Lai, G. Ning, H. Zhang, J. Power Sources 266 (2014) 145–149.

[10] Y. Yao, J. Lei, Y. Shi, F. Ai, Y.-C. Lu, Nat Energy 6 (2021) 582–588. https://doi.org/10.1038/s41560-020-00772-8.

[11] V. Singh, S. Kim, J. Kang, H.R. Byon, Nano Res. 12 (2019) 1988–2001. https://doi.org/10.1007/s12274-019-2355-2.

[12] J. Winsberg, T. Hagemann, T. Janoschka, M.D. Hager, U.S. Schubert, Angew. Chem. Int. Ed. Engl. 56 (2017) 686–711. https://doi.org/10.1002/anie.201604925.

[13] Q. Xu, Y.N. Ji, L.Y. Qin, P.K. Leung, F. Qiao, Y.S. Li, H.N. Su, Journal of Energy Storage 16 (2018) 108–115. https://doi.org/10.1016/j.est.2018.01.005.

[14] L.H. Thaller, Electrically rechargeable redox flow cell, 1975, accessed 12 May 2020.

[15] M. Bartolozzi, J. Power Sources 27 (1989) 219–234.

[16] L. Cao, M. Skyllas-Kazacos, C. Menictas, J. Noack, Journal of Energy Chemistry 27 (2018) 1269–1291. https://doi.org/10.1016/j.jechem.2018.04.007.

[17] C. Choi, S. Kim, R. Kim, Y. Choi, S. Kim, H. Jung, J.H. Yang, H.-T. Kim, Renewable and Sustainable Energy Reviews 69 (2017) 263–274. https://doi.org/10.1016/j.rser.2016.11.188.

[18] Á. Cunha, J. Martins, N. Rodrigues, F.P. Brito, Int. J. Energy Res. 39 (2015) 889–918. https://doi.org/10.1002/er.3260.

[19] M. Gencten, Y. Sahin, Int J Energy Res 451 (2020) 629. https://doi.org/10.1002/er.5487.

[20] G. Kear, A.A. Shah, F.C. Walsh, Int J Energy Res 36 (2012) 1105–1120. https://doi.org/10.1002/er.1863.

[21] A. Parasuraman, T.M. Lim, C. Menictas, M. Skyllas-Kazacos, Electrochim. Acta 101 (2013) 27–40. https://doi.org/10.1016/j.electacta.2012.09.067.

[22] M. Skyllas-Kazacos, L. Cao, M. Kazacos, N. Kausar, A. Mousa, ChemSusChem 9 (2016) 1521–1543. https://doi.org/10.1002/cssc.201600102.

[23] M. Skyllas-Kazacos, G. Kazacos, G. Poon, H. Verseema, Int. J. Energy Res. 34 (2010) 182–189.

[24] C. Blanc, A. Rufer, in: Paths to Sustainable Energy. Dr Artie Ng, 2010, pp. 334–358.

[25] M. Skyllas-Kazacos, All-vanadium redox flow battery, 1988, accessed 13 January 2020.

[26] E. Sum, M. Rychcik, M. Skyllas-Kazacos, J. Power Sources 16 (1985) 85–95.

[27] Z. Li, Y.-C. Lu, Adv. Mater. 32 (2020) e2002132. https://doi.org/10.1002/adma.202002132.

[28] Y. Xu, Y. Wen, J. Cheng, Y. Yanga, Z. Xie, G. Cao, in: 2009 World Non-Grid-Connected Wind Power and Energy Conference (WNWEC 2009), pp. 1–4.

[29] P. Leung, A.A. Shah, L. Sanz, C. Flox, J.R. Morante, Q. Xu, M.R. Mohamed, Ponce de León, C., F.C. Walsh, J. Power Sources 360 (2017) 243–283. https://doi.org/10.1016/j.jpowsour.2017.05.057.

[30]   R.M. Darling, K.G. Gallagher, J.A. Kowalski, S. Ha, F.R. Brushett, Energy Environ. Sci. 7 (2014) 3459–3477. https://doi.org/10.1039/C4EE02158D.

[31]   A.A. Shah, M.J. Watt-Smith, F.C. Walsh, Electrochim. Acta 53 (2008) 8087–8100. https://doi.org/10.1016/j.electacta.2008.05.067.

[32]   W. Wang, V. Sprenkle, Nat Chem 8 (2016) 204–206.

[33]   J. Luo, A. Sam, B. Hu, C. DeBruler, X. Wei, W. Wang, T.L. Liu, Nano Energy 42 (2017) 215–221. https://doi.org/10.1016/j.nanoen.2017.10.057.

[34]   Y. Ding, Y. Zhao, Y. Li, J.B. Goodenough, G. Yu, Energy Environ. Sci. (2016). https://doi.org/10.1039/C6EE02057G.

[35]   Y.-K. Han, C.-S. Jin, Current Applied Physics 18 (2018) 1507–1512. https://doi.org/10.1016/j.cap.2018.09.007.

[36]   C.L. Bird, A.T. Kuhn, Chem. Soc. Rev. (1981) 49–82.

[37]   J.E. Nutting, M. Rafiee, S.S. Stahl, Chemical reviews 118 (2018) 4834–4885. https://doi.org/10.1021/acs.chemrev.7b00763.

[38]   A. Hollas, X. Wei, V. Murugesan, Z. Nie, B. Li, D. Reed, J. Liu, V. Sprenkle, W. Wang, Nat Energy 3 (2018) 508–514. https://doi.org/10.1038/s41560-018-0167-3.

[39]   K. Lin, R. Gómez-Bombarelli, E.S. Beh, L. Tong, Q. Chen, A. Valle, A. Aspuru-Guzik, M.J. Aziz, R.G. Gordon, Nat. Energy 1 (2016) 16102. https://doi.org/10.1038/nenergy.2016.102.

[40]   B. Yang, L. Hoober-Burkhardt, S. Krishnamoorthy, A. Murali, Prakash, G. K. Surya, S.R. Narayanan, J. Electrochem. Soc. 163 (2016) A1442-A1449. https://doi.org/10.1149/2.1371607jes.

[41]   K. Lin, Q. Chen, M.R. Gerhardt, L. Tong, S.B. Kim, L. Eisenach, A.W. Valle, D. Hardee, R.G. Gordon, M.J. Aziz, M.P. Marshak, Science 349 (2015) 1529–1532. https://doi.org/10.1126/science.aab3033.

[42]   Y. Ji, M.-A. Goulet, D.A. Pollack, D.G. Kwabi, S. Jin, D. de Porcellinis, E.F. Kerr, R.G. Gordon, M.J. Aziz, Advanced Energy Materials 9 (2019). https://doi.org/10.1002/aenm.201900039.

[43]   T. Liu, X. Wei, Z. Nie, V. Sprenkle, W. Wang, Adv. Energy Mater. 6 (2016) 1501449. https://doi.org/10.1002/aenm.201501449.

[44]   E.S. Beh, D. de Porcellinis, R.L. Gracia, K.T. Xia, R.G. Gordon, M.J. Aziz, ACS Energy Lett. 2 (2017) 639–644. https://doi.org/10.1021/acsenergylett.7b00019.

[45]   J. Luo, B. Hu, C. DeBruler, Y. Bi, Y. Zhao, B. Yuan, M. Hu, W. Wu, T.L. Liu, Joule 3 (2019) 149–163. https://doi.org/10.1016/j.joule.2018.10.010.

[46]   M.H. Chakrabarti, N.P. Brandon, S.A. Hajimolana, F. Tariq, V. Yufit, M.A. Hashim, M.A. Hussain, C. Low, P.V. Aravind, J. Power Sources 253 (2014) 150–166.

[47]   I. Derr, D. Przyrembel, J. Schweer, A. Fetyan, J. Langner, J. Melke, M. Weinelt, C. Roth, Electrochimica Acta 246 (2017) 783–793. https://doi.org/10.1016/j.electacta.2017.06.050.

[48]   I. Derr, M. Bruns, J. Langner, A. Fetyan, J. Melke, C. Roth, J. Power Sources 325 (2016) 351–359. https://doi.org/10.1016/j.jpowsour.2016.06.040.

[49]   I. Derr, Electrochemical degradation and chemical aging of carbon felt electrodes in all-vanadium redox flow batteries, Berlin, 2017.

[50]   N. Macauley, D.D. Papadias, D. Spernjak, D. Langlois, R. Ahluwalia, K.L. More, R. Mukundan, R.L. Borup, J.Electrochem.Soc. 165 (2018) 3148–3160.

[51]   M. Nourani, B.I. Zackin, D.C. Sabarirajan, R. Taspinar, K. Artyushkova, F. Liu, I.V. Zenyuk, E. Agar, J.Electrochem.Soc. 166 (2019) A353-A363.

[52]   X.-Z. Yuan, C. Song, A. Platt, N. Zhao, H. Wang, H. Li, K. Fatih, D. Jang, Int J Energy Res 50 (2019) 88. https://doi.org/10.1002/er.4607.

[53]   A. COLLIER, H. WANG, X. ZIYUAN, J. ZHANG, D. WILKINSON, International Journal of Hydrogen Energy 31 (2006) 1838–1854. https://doi.org/10.1016/j.ijhydene.2006.05.006.

[54]   C. Chen, T.F. Fuller, Electrochim. Acta 54 (2009) 3984–3995. https://doi.org/10.1016/j.electacta.2009.02.021.

[55]   T. Xie, C.A. Hayden, Polymer 48 (2007) 5497–5506. https://doi.org/10.1016/j.polymer.2007.07.043.

[56] L. Ghassemzadeh, T.J. Peckham, T. Weissbach, X. Luo, S. Holdcroft, Journal of the American Chemical Society 135 (2013) 15923–15932. https://doi.org/10.1021/ja408032p.

[57] T. Sukkar, M. Skyllas-Kazacos, J. Membr. Sci. 222 (2003) 235–247.

[58] K. Oh, M. Moazzam, G. Gwak, H. Ju, Electrochimica Acta 297 (2019) 101–111. https://doi.org/10.1016/j.electacta.2018.11.151.

[59] L.J. Small, H.D. Pratt, T.M. Anderson, J.Electrochem.Soc. 166 (2019) 2536–2542.

[60] D.G. Kwabi, Y. Ji, M.J. Aziz, Chemical reviews (2020). https://doi.org/10.1021/acs.chemrev.9b00599.

[61] C.A.P. Arellano, S.S. Martínez, Solar Energy Materials and Solar Cells 94 (2010) 327–332. https://doi.org/10.1016/j.solmat.2009.10.008.

[62] K. Kunimatsu, Y. Shigematsu, K. Uosaki, H. Kita, Journal of Electroanalytical Chemistry 262 (1989) 195–209.

[63] D.D. Kuhn, T.C. Young, Chemosphere 60 (2005) 1222–1230. https://doi.org/10.1016/j.chemosphere.2005.02.011.

[64] M. Cazot, G. Maranzana, J. Dillet, F. Beille, T. Godet-Bar, S. Didierjean, Electrochimica Acta 321 (2019) 134705. https://doi.org/10.1016/j.electacta.2019.134705.

[65] M. Cazot, Development of Analytical Techniques for the Investigation of an Organic Redox flow Battery using a Segmented Cell. PhD, Nancy, 2019.

[66] I. M. Kolthoff and E. A. Pearson, Ind. Eng. Chem. Res. 3 (1931).

[67] T. Páez, A. Martínez-Cuezva, R. MARCILLA, J. Palma, E. Ventosa, J. Power Sources 512 (2021) 230516. https://doi.org/10.1016/j.jpowsour.2021.230516.

[68] G. Zotti, G. Schiavon, S. Zecchin, D. Favretto, Journal of Electroanalytical Chemistry 456 (1998) 217–221.

[69] R. Prins, A.R. Korswagen, Kortbeek, A. G. T. G., Journal of Organometallic Chemistry 39 (1972) 335–344.

[70] A. Kutyrev, Tetrahedron 47 (1991) 8043–8065.

[71] A. Murali, A. Nirmalchandar, S. Krishnamoorthy, L. Hoober-Burkhardt, B. Yang, G.L. Soloveichik, Surya Prakash, G. K., A. Narayanan, J. Electrochem. Soc. 165 (2018) 1193–1203.

[72] A. Brunmark, E. Cadenas, Free radical biology & medicine 3 (1987) 169–180.

[73] M.-A. Goulet, L. Tong, D.A. Pollack, D.P. Tabor, S.A. Odom, A. Aspuru-Guzik, E.E. Kwan, R.G. Gordon, M.J. Aziz, Journal of the American Chemical Society (2019). https://doi.org/10.1021/jacs.8b13295.

[74] D.P. Tabor, R. Gómez-Bombarelli, L. Tong, R.G. Gordon, M.J. Aziz, A. Aspuru-Guzik, J. Mater. Chem. A 7 (2019) 12833–12841. https://doi.org/10.1039/C9TA03219C.

[75] L. Hoober-Burkhardt, S. Krishnamoorthy, B. Yang, A. Murali, A. Nirmalchandar, Prakash, G. K. Surya, S.R. Narayanan, J. Electrochem. Soc. 164 (2017) A600-A607. https://doi.org/10.1149/2.0351704jes.

[76] J. Rubio-Garcia, A. Kucernak, A. Parra-Puerto, R. Liu, B. Chakrabarti, J. Mater. Chem. A 8 (2020) 3933–3941. https://doi.org/10.1039/C9TA12396B.

[77] K. Wedege, E. Dražević, D. Konya, A. Bentien, Scientific reports 6 (2016) srep39101. https://doi.org/10.1038/srep39101.

[78] T.J. Carney, S.J. Collins, J.S. Moore, F.R. Brushett, Chem. Mater. 29 (2017) 4801–4810. https://doi.org/10.1021/acs.chemmater.7b00616.

[79] C. Wiberg, T.J. Carney, F. Brushett, E. Ahlberg, E. Wang, Electrochim. Acta 317 (2019) 478–485. https://doi.org/10.1016/j.electacta.2019.05.134.

[80] F. Beck, G. Heydecke, Berichte der Bunsengesellschaft für physikalische Chemie 91 (1987) 37–43.

[81] E.W. Zhao, E. Jónsson, R.B. Jethwa, D. Hey, D. Lyu, A. Brookfield, P.A.A. Klusener, D. Collison, C.P. Grey, J. Am. Chem. Soc. 143 (2021) 1885–1895. https://doi.org/10.1021/jacs.0c10650.

[82] D.G. Kwabi, K. Lin, Y. Ji, E.F. Kerr, M.-A. Goulet, D. de Porcellinis, D.P. Tabor, D.A. Pollack, A. Aspuru-Guzik, R.G. Gordon, M.J. Aziz, Joule 2 (2018) 1894–1906. https://doi.org/10.1016/j.joule.2018.07.005.

[83] D.L. Marshall, M.L. Christian, G. Gryn'ova, M.L. Coote, P.J. Barker, S.J. Blanksby, Organic & biomolecular chemistry 9 (2011) 4936–4947. https://doi.org/10.1039/c1ob05037k.

[84] A. Nilsen, R. Braslau, J. Polym. Sci. A Polym. Chem. 44 (2006) 697–717. https://doi.org/10.1002/pola.21207.

[85]   Judith R. Fish/Steven G. Swarts/Michael D. Sevilla/Tadeusz Malinski.

[86]   W. Zhou, W. Liu, M. Qin, Z. Chen, J. Xu, J. Cao, J. Li, RSC Adv. 10 (2020) 21839–21844. https://doi.org/10.1039/D0RA03424J.

[87]   B. Hu, Y. Tang, J. Luo, G. Grove, Y. Guo, T.L. Liu, Chemical communications (Cambridge, England) 54 (2018) 6871–6874. https://doi.org/10.1039/c8cc02336k.

[88]   J.A. Farrington, Chem. Commun. (1969) 259–260.

[89]   Catherine D. Clark, †, Jeff D. Debad, Edward H. Yonemoto, ‡, Thomas E. Mallouk, ‡ and, and Allen J. Bard*.

[90]   Q. Chen, L. Eisenach, M.J. Aziz, J. Electrochem. Soc. 163 (2015) A5057-A5063. https://doi.org/10.1149/2.0081601jes.

[91]   Y.A. Gandomi, D.S. Aaron, J.R. Houser, M.C. Daugherty, J.T. Clement, A.M. Pezeshki, T.Y. Ertugrul, D.P. Moseley, M.M. Mench, J. Electrochem. Soc. 165 (2018) A970-A1010. https://doi.org/10.1149/2.0601805jes.

[92]   Y. Peng, J.-Y. Choi, K. Bai, Y. Zhang, D. Banham, J. Power Sources 500 (2021) 229986. https://doi.org/10.1016/j.jpowsour.2021.229986.

[93]   S. Saxena, D. Roman, V. Robu, D. Flynn, M. Pecht, Energies 14 (2021) 723. https://doi.org/10.3390/en14030723.

[94]   A.M. Pezeshki, R.L. Sacci, G.M. Veith, T.A. Zawodzinski, M.M. Mench, J. Electrochem. Soc. 163 (2016) A5202-A5210. https://doi.org/10.1149/2.0251601jes.

[95]   M.-A. Goulet, M.J. Aziz, J. Electrochem. Soc. 165 (2018) A1466-A1477. https://doi.org/10.1149/2.0891807jes.

[96]   S. Jin, E.M. Fell, L. Vina-Lopez, Y. Jing, P.W. Michalak, R.G. Gordon, M.J. Aziz, Adv. Energy Mater. 10 (2020) 2000100. https://doi.org/10.1002/aenm.202000100.

[97]   D. Aaron, Z. Tang, A.B. Papandrew, T.A. Zawodzinski, J. Appl. Electrochem. 41 (2011) 1175–1182. https://doi.org/10.1007/s10800-011-0335-7.

[98]   C. Liu, W. Liu, L. Wang, G. Hu, L. Ma, B. Ren, J. Power Sources 320 (2016) 1–12. https://doi.org/10.1016/j.jpowsour.2016.03.112.

[99]   L. Tong, Q. Chen, A.A. Wong, R. Gómez-Bombarelli, A. Aspuru-Guzik, R.G. Gordon, M.J. Aziz, Physical chemistry chemical physics PCCP 19 (2017) 31684–31691. https://doi.org/10.1039/c7cp05881k.

[100]   O. Nolte, R. Geitner, M.D. Hager, U.S. Schubert, Adv. Energy Mater. (2021) 2100931. https://doi.org/10.1002/aenm.202100931.

[101]   E.W. Zhao, T. Liu, E. Jónsson, J. Lee, I. Temprano, R.B. Jethwa, A. Wang, H. Smith, J. Carretero-González, Q. Song, C.P. Grey, Nature 579 (2020) 224–228. https://doi.org/10.1038/s41586-020-2081-7.

[102]   R. Petrone, Z. Zheng, D. Hissel, M.C. Péra, C. Pianese, M. Sorrentino, M. Becherif, N. Yousfi-Steiner, International Journal of Hydrogen Energy 38 (2013) 7077–7091. https://doi.org/10.1016/j.ijhydene.2013.03.106.

[103]   S. Abada, M. Petit, A. Lecocq, G. Marlair, V. Sauvant-Moynot, F. Huet, Journal of Power Sources 399 (2018) 264–273. https://doi.org/10.1016/j.jpowsour.2018.07.094.

[104]   A.A. Shah, H. Al-Fetlawi, F.C. Walsh, Electrochim. Acta 55 (2010) 1125–1139. https://doi.org/10.1016/j.electacta.2009.10.022.

[105]   B. Xiong, Y. Yang, J. Tang, Y. Li, Z. Wei, Y. Su, Q. Zhang, IEEE Access 7 (2019) 162297–162308. https://doi.org/10.1109/ACCESS.2019.2952212.

[106]   Y. Zhang, J. Zhao, P. Wang, M. Skyllas-Kazacos, B. Xiong, R. Badrinarayanan, Journal of Power Sources 290 (2015) 14–24. https://doi.org/10.1016/j.jpowsour.2015.04.169.

[107]   A. Bhattacharjee, A. Roy, N. Banerjee, S. Patra, H. Saha, J. Power Sources 396 (2018) 506–518. https://doi.org/10.1016/j.jpowsour.2018.06.017.

[108]   Al-Fetlawi, Hassan Abdul-Zehra Abdul-Yima, A.A. Shah, F.C. Walsh, Electrochim. Acta 55 (2009) 78–89. https://doi.org/10.1016/j.electacta.2009.08.009.

[109]   C. Yin, Y. Gao, G. Xie, T. Li, H. Tang, Journal of Power Sources 438 (2019) 227023. https://doi.org/10.1016/j.jpowsour.2019.227023.

[110]   M. Petit, M. Leroy, P. Jacquinet, D. Audigier, D. Pasquier, in: The International Flow Battery Forum.

[111]   C. Zhang, Z. Niu, S. Peng, Y. Ding, L. Zhang, X. Guo, Y. Zhao, G. Yu, Advanced Materials 31 (2019). https://doi.org/10.1002/adma.201901052.

[112]   S. Er, C. Suh, M.P. Marshak, A. Aspuru-Guzik, Chem. Sci. 6 (2015) 885–893. https://doi.org/10.1039/c4sc03030c.

[113]   D. Wang, S. Huang, C. Wang, Y. Yue, Q. Zhang, Organic Electronics 64 (2019) 216–222. https://doi.org/10.1016/j.orgel.2018.10.038.

[114]   Z. Jiang, K. Klyukin, V. Alexandrov, ACS applied materials & interfaces 10 (2018) 20621–20626. https://doi.org/10.1021/acsami.8b05864.

[115]   M. Zago, A. Casalegno, Electrochim. Acta 248 (2017) 505–517. https://doi.org/10.1016/j.electacta.2017.07.166.

[116]   K.W. Knehr, E. Agar, C.R. Dennison, A.R. Kalidindi, E.C. Kumbur, J. Electrochem. Soc. 159 (2012) A1446-A1459. https://doi.org/10.1149/2.017209jes.

[117]   M. LI, T. Hikihara, IEICE Transactions on Fundamentals of Electronics, Communications and Computer Sciences E91-A (2008) 1741–1747. https://doi.org/10.1093/ietfec/e91-a.7.1741.

[118]   C. Blanc, Modeling of a vanadium redox flow battery electricity storage system, 2009.

[119]   G. Merei, S. Adler, D. Magnor, D.U. Sauer, Electrochimica Acta 174 (2015) 945–954. https://doi.org/10.1016/j.electacta.2015.06.046.

[120]   Q. Xu, T.S. Zhao, Progress in Energy and Combustion Science 49 (2015) 40–58. https://doi.org/10.1016/j.pecs.2015.02.001.

[121]   X. Li, Electrochimica Acta 170 (2015) 98–109. https://doi.org/10.1016/j.electacta.2015.04.075.

[122]   Al-Fetlawi, Hassan Abdul-Zehra Abdul-Yima, Modelling and simulation of all-vanadium redox flow batteries. PhD, University of Southampton, 2011.

[123]   M. Belchuk, S. Wagener, J. Zabold, 293 - Sealing PEM Fuel Cells - 2011 FC Seminar 2011-10-07, 2011.

[124]   R. Byron Bird, E.W. Steward, E.N. Lightfoot, Transport phenomena: Second Edition, John Wiley & Sons, Inc, NY, 2002.

[125]   D.M. Bernardi, M.W. Verbrugge, J. Electrochem. Soc. 139 (1992) 2477–2491.

[126]   L. Hao, Y. Wang, Y. He, Journal of The Electrochemical Society 166 (2019) A1310-A1322. https://doi.org/10.1149/2.1061906jes.

[127]   E. Fried, I.E. Idelchik (Eds.), Handbook of hydraulic resistance, 2nd ed., rev. and augm, Hemisphere Pub. Corp, Washington, 1986.

[128]   H. Al-Fetlawi, A.A. Shah, F.C. Walsh, Electrochim. Acta 55 (2010) 3192–3205. https://doi.org/10.1016/j.electacta.2009.12.085.

[129]   C.R. Birkl, M.R. Roberts, E. McTurk, P.G. Bruce, D.A. Howey, Journal of Power Sources 341 (2017) 373–386. https://doi.org/10.1016/j.jpowsour.2016.12.011.

[130]   M. Yue, S. Jemei, R. Gouriveau, N. Zerhouni, International Journal of Hydrogen Energy 44 (2019) 6844–6861. https://doi.org/10.1016/j.ijhydene.2019.01.190.

[131]   M. Skyllas-Kazacos, L. Goh, Journal of Membrane Science 399-400 (2012) 43–48. https://doi.org/10.1016/j.memsci.2012.01.024.

[132]   P.A. Boettcher, E. Agar, C.R. Dennison, E.C. Kumbur, J. Electrochem. Soc. 163 (2015) A5244-A5252. https://doi.org/10.1149/2.0311601jes.

[133]   Q. Cacciuttolo, M. Petit, D. Pasquier, Electrochim. Acta (2021) 138961. https://doi.org/10.1016/j.electacta.2021.138961.

[134]   S. Modak, D.G. Kwabi, Journal of The Electrochemical Society 168 (2021) 80528. https://doi.org/10.1149/1945-7111/ac1c1f.

[135]   M.M. Saleh, J Solid State Electrochem 11 (2007) 811–820. https://doi.org/10.1007/s10008-006-0227-7.

[136]   Y. Ji, F. Zhang, M. Zhou, J. Yu, Q. Wang, International Journal of Hydrogen Energy 45 (2020) 18888–18894. https://doi.org/10.1016/j.ijhydene.2020.05.129.

[137]   S. Abada, G. Marlair, A. Lecocq, M. Petit, V. Sauvant-Moynot, F. Huet, J. Power Sources 306 (2016) 178–192. https://doi.org/10.1016/j.jpowsour.2015.11.100.

[138]   F. Huet, Journal of Power Sources 70 (1998) 59–69.

[139]   Q. Yang, J. Xu, X. Li, D. Xu, B. Cao, International Journal of Electrical Power & Energy Systems 119 (2020) 105883. https://doi.org/10.1016/j.ijepes.2020.105883.

[140]   M. Becherif, M.-C. Péra, D. Hissel, Z. Zheng, Journal of Cleaner Production 171 (2018) 1510–1519. https://doi.org/10.1016/j.jclepro.2017.10.072.

[141]   D. Zhang, P. Baraldi, C. Cadet, N. Yousfi-Steiner, C. Bérenguer, E. Zio, Mechanical Systems and Signal Processing 124 (2019) 479–501. https://doi.org/10.1016/j.ymssp.2019.01.060.